Analytic systematics in next generation of effective-one-body gravitational waveform models for future observations

Alessandro Nagar,[1,2] Piero Rettegno,[1] Rossella Gamba,[3] Simone Albanesi,[1] Angelica Albertini,[4,5] and Sebastiano Bernuzzi[3]

[1]*INFN Sezione di Torino, Via P. Giuria 1, 10125 Torino, Italy*
[2]*Institut des Hautes Etudes Scientifiques, 91440 Bures-sur-Yvette, France*
[3]*Theoretisch-Physikalisches Institut, Friedrich-Schiller-Universität Jena, 07743, Jena, Germany*
[4]*Astronomical Institute of the Czech Academy of Sciences, Boční II 1401/1a, CZ-141 00 Prague, Czech Republic*
[5]*Faculty of Mathematics and Physics, Charles University in Prague, 18000 Prague, Czech Republic*

(Received 20 April 2023; revised 11 September 2023; accepted 14 September 2023; published 6 December 2023)

The success of analytic waveform modeling within the effective-one-body (EOB) approach relies on the precise understanding of the physical importance of each technical element included in the model. The urgency of constructing progressively more sophisticated and complete waveform models (e.g. including spin precession and eccentricity) partly defocused the research from a careful comprehension of each building block (e.g. Hamiltonian, radiation reaction, ringdown attachment). Here we go back to the spirit of the first EOB works. We focus first on nonspinning, quasicircular, black hole binaries and analyze systematically the mutual synergy between numerical relativity (NR) informed functions and the high post-Newtonian corrections (up to 5PN) to the EOB potentials. Our main finding is that it is essential to correctly control the noncircular part of the dynamics during the late plunge up to merger. When this happens, either using NR-informed nonquasicircular corrections to the waveform (and flux) or high-PN corrections in the radial EOB potentials (D, Q), it is easy to obtain EOB/NR unfaithfulness $\sim 10^{-4}$ with the noise of either Advanced LIGO or 3G detectors. We then improve the TEOBResumS-GIOTTO waveform model (dubbed TEOBResumSv4.3.2) for quasicircular, spin-aligned black hole binaries. We obtain maximal EOB/NR unfaithfulness $\bar{\mathcal{F}}^{\max}_{\mathrm{EOBNR}} \sim 10^{-3}$ (with Advanced LIGO noise and in the total mass range 10–$200 M_\odot$) for the dominant $\ell = m = 2$ mode all over the 534 spin-aligned configurations available through the Simulating eXtreme Spacetime catalog. The model performance, also including higher modes, is then explored using the NR surrogates NRHybSur3dq8 and NRHybSur2dq15, to validate TEOBResumSv4.3.2 up to mass ratio $m_1/m_2 = 15$. We find that, over the set of configurations considered, more than 98% of the total-mass-maximized unfaithfulness lie below the 3% threshold when comparing to the surrogate models.

DOI: 10.1103/PhysRevD.108.124018

I. INTRODUCTION

With the ever-growing sensitivities of gravitational wave (GW) observatories, the issue of systematic errors due to modeling is at the forefront of GW astronomy. This topic has received some attention in the recent literature [1–5], and such errors are typically quantified in terms of their impact on parameter estimation, and studied by comparing the posterior distributions obtained with different models. Unfortunately, so far only few studies have attempted to link the observed differences to the specifics of the models themselves, in large part due to their extreme complexity, which stems from the need of describing a large class of systems and physical effects.

In this respect, the effective-one-body (EOB) [6–9] approach to the general relativistic two-body problem is currently the only formalism sufficiently flexible and accurate to generate reliable waveforms for any kind of coalescing binaries, from quasicircular and eccentric black holes [10–19], to neutron stars [3,16,20–23] or mixed binaries [24,25]. This framework is characterized by a few, well defined, building blocks (i.e. Hamiltonian, radiation reaction, waveform, ringdown description) that can incorporate a variable amount of analytic information—usually post-Newtonian results repackaged in some resummed fashion—suitably augmented by numerical relativity (NR) information.

Within the EOB approach, the issue of understanding waveform systematics rephrases as the need of evaluating the impact that each (sub)building block of the model may have on waveform accuracy.[1] This conceptual approach

[1]This waveform accuracy is typically evaluated using phasing comparisons with NR waveform data, considered as exact for any practical purpose.

was followed in, e.g., Refs. [26–29], and was essential to identify the best analytical waveform description through plunge up to merger. Note that this effort was nontrivial, as the flexibility of the framework implies some degree of arbitrariness in, e.g., resummation choices. We then define "analytic" waveform systematics all errors stemming from the choices in the analytic structure of a model. In recent years, the rush of constructing physically complete EOB waveform models, to satisfy the needs of gravitational wave data analysis, partly defocused the current EOB research from the scope of minimizing analytic systematics, and deeply understanding the interplay of the various analytical elements with each other and with the procedure of *calibrating* the analytical model. Here we make an effort to go back to the original EOB philosophy [26–29]. We attempt to understand, one by one, the influence of various building elements of the Hamiltonian, or other well-defined and established procedure, like the determination of next-to-quasicircular (NQC) to the waveform and radiation reaction. This knowledge allows then to better clarify which directions to follow aiming at improved waveform accuracy for next generation detectors like Einstein Telescope [30–32] and Cosmic Explorer [33].

The paper is organized as follows. In Sec. II we present an improved nonspinning sector of TEOBResumS via a more precise NR-informed effective-5PN function a_6^c. Using this model as a reference baseline, in Sec. III we explore various analytic systematics, like the effect of changing the ringdown matching point and the inclusion of high-order (noncircular) terms in the EOB potentials. This allows the construction of different quasicircular EOB waveform models with different analytic content and related levels of EOB/NR unfaithfulness. To enlarge our battery of EOB models, and related analytic systematics, in Sec. IV we present an upgrade of the eccentric EOB model of Ref. [34], which offers a better performance either for quasicircular binaries or for scattering angle. In Sec. V we complement the newly determined $a_6^c(\nu)$ function of Sec. II with progressively different NR-informed spin-orbit sectors. This eventually brings us to the construction of a new, spin-aligned, waveform model for quasicircular binaries (including higher modes) that performs better than the state-of-the-art TEOBResumS. In particular, here we also incorporate within TEOBResumS the description of the ringdown of the $\ell = 2$, $m = 1$ mode that is part of the SEOBNRv5 model [35]. This allows us to eliminate long-standing issues due to the bad modelization of this mode in the standard TEOBResumS construction [36]. The notation and analytical information of this paper strongly builds upon Refs. [14,34,36], and we assume the reader to be familiar with the content and notation of those papers. We only recall a few notational elements: (m_1, m_2) are the masses of the two black holes, with $q = m_1/m_2 \geq 1$ the mass ratio, $M \equiv m_1 + m_2$ the total mass and $\nu \equiv m_1 m_2/M^2$ the symmetric mass ratio and $X_i \equiv m_i/M$ with $i = 1, 2$. The dimensionless spin magnitudes are $\chi_i \equiv S_i/m_1^2$ with $i = 1, 2$, and we indicate with $\tilde{a}_0 \equiv X_1\chi_1 + X_2\chi_2$ the effective spin, usually indicated as $\chi_{\rm eff}$ in the literature. If not stated otherwise, we use geometric units with $c = G = 1$.

II. IMPROVING THE CONSERVATIVE NONSPINNING SECTOR OF TEOBResumS-GIOTTO

The nonspinning Hamiltonian of TEOBResumS-GIOTTO (only TEOBResumS in the following for simplicity) depends on a single NR-informed function $a_6^c(\nu)$, which plays the role of an effective 5PN correction in the EOB radial potential $A(r)$ [29], where $r \equiv R/M$ is the dimensionless relative separation between the two bodies. The original function $a_6^c(\nu)$ employed in TEOBResumS dates back to Ref. [37], and, for simplicity, was never changed since (see in particular Table I of [37] and related simulations of the Simulating eXtreme Spacetimes (SXS) catalog [38–51] used to determine it). This expression of $a_6^c(\nu)$ was rather conservative, allowing for EOB/NR phase differences of the same order of (or larger than) the nominal NR phase uncertainty at merger. The latter is typically defined, for a given simulation, as the phase difference between the highest and second highest resolutions available in the SXS catalog. This uncertainty estimate, however, is quite conservative on average,[2] and may not properly reflect systematic effects affecting the NR waveform (see, e.g., Ref [36] for some discussions). Therefore, in this work we *assume* that the uncertainty on the highest resolution available is substantially negligible. For each dataset, we tune a_6^c so to have an accumulated EOB/NR phase difference that is as small as possible at NR merger (say, $\lesssim$0.05 rad) and moreover (mostly) decreases *monotonically.* This qualitative feature of the phase difference is *crucial* to obtain EOB/NR unfaithfulness of a few parts in $\sim 10^{-4}$, as we will see below.[3] Here we determine a_6^c pointwise using the SXS datasets listed in Table I. The raw values can be accurately fitted versus ν with the usual rational function,

$$a_6^c = n_0 \frac{1 + n_1\nu + n_2\nu^2 + n_3\nu^3}{1 + d_1\nu}, \tag{1}$$

with the coefficients listed in Table II under `D3Q3_NQC`.

[2]Note in passing that this is a property of the SpEC code. Though finite-difference codes give results that are in general less accurate during the inspiral, at least one can extrapolate to infinite resolution and get a sense of the uncertainties due to finite resolution. See for example [52].

[3]In previous EOB models, see for example Refs. [53,54], we NR informed the EOB model aiming at 10^{-2} EOB/NR unfaithfulness only. This is easily reachable also in case the phase difference is not monotonic but oscillates around merger, see for example Fig. 1 of [53].

TABLE I. Nonspinning SXS simulations used in the first part of the paper to construct and check the various EOB nonspinning models characterized in Table II. They are selected as nonspinning because the initial effective spin of the system, $\tilde{a}_0$ is smaller than 10^{-6}. Only some datasets are used to determine the first-guess values of a_6^c, then fitted with functional forms and coefficients also listed in Table II. All datasets are then used to validate the models, either with time-domain phasing comparisons or EOB/NR unfaithfulness calculations. The fifth column reports the nominal NR phasing uncertainty at merger $\delta\phi^{\rm NR}_{\rm mrg}$, obtained by taking the phase difference between the highest and second highest resolutions available.

					a_6^c first-guess values				
No.	SXS	q	ν	$\delta\phi^{\rm NR}_{\rm mrg}$ [rad]	D3Q3_NQC	D5Q5_NQC	D5Q5	D3Q3	D5Q3
1	SXS:BBH:0180	1	0.25	+0.42	−36.0	−98.0	−5	11	−13
2	SXS:BBH:0007	1.5	0.24	−0.0186	−41.5	−92.0	−15	13	−13.5
3	SXS:BBH:0169	2	$0.\bar{2}$	−0.0271	−48.0	−81.5	−29	15	−15
4	SXS:BBH:0259	2.5	0.2041	+0.0080	⋯	⋯	−31	⋯	⋯
5	SXS:BBH:0168	3	0.1875	+0.1144	−51.0	−68.0	−30.2	17	−19
6	SXS:BBH:0294	3.5	0.1728	+1.325	⋯	⋯	−29.2	⋯	⋯
7	SXS:BBH:0295	4.5	0.1488	−0.240	−45.0	−54.0	−28.5	14.5	−17
8	SXS:BBH:0056	5	0.1389	−0.439	⋯	⋯	−27.7	⋯	⋯
9	SXS:BBH:0296	5.5	0.1302	−0.443	⋯	⋯	⋯	⋯	⋯
10	SXS:BBH:0166	6	0.1224	⋯	⋯	⋯	⋯	⋯	⋯
11	SXS:BBH:0297	6.5	0.1156	−0.053	−34.5	−42.0	−26	11	−12
12	SXS:BBH:0298	7	0.1094	+0.078	−31.5	−39.5	−25	10	−11
13	SXS:BBH:0299	7.5	0.1038	+0.050	⋯	⋯	⋯	⋯	⋯
14	SXS:BBH:0063	8	0.0988	−1.009	⋯	⋯	⋯	⋯	⋯
15	SXS:BBH:0301	9	0.090	+0.16	⋯	⋯	⋯	⋯	⋯
16	SXS:BBH:0302	9.5	0.0826	−0.020	−19.5	−25.9	−14	8.5	−8

Figure 1 shows a sample of EOB/NR time-domain phasings obtained using this expression of $a_6^c(\nu)$. Following our usual habits, the figure depicts the Regge-Wheeler-Zerilli normalized quadrupolar waveform Ψ_{22} that is connected to the (otherwise commonly used) strain multipoles $h_{\ell m}$ as $\Psi_{\ell m} \equiv h_{\ell m}/\sqrt{(\ell+2)(\ell+1)\ell(\ell-1)}$, where

$$h_+ - ih_\times = \frac{1}{\mathcal{D}_L}\sum_{\ell=2}^{\infty}\sum_{m=-\ell}^{\ell} h_{\ell m}\,{}_{-2}Y_{\ell m}, \tag{2}$$

with $\mathcal{D}_L$ as the luminosity distance and ${}_{-2}Y_{\ell m}$ are the $s=-2$ spin-weighted spherical harmonics. The waveform Ψ_{22} is then decomposed in amplitude and phase as $\Psi_{22} = A_{22}e^{-i\phi_{22}}$. Following standard procedures, the EOB and NR waveforms are aligned by applying an arbitrary time and phase shift, obtained following the standard procedure delineated in, e.g., Ref. [55]. Note that, to maximize accuracy, this comparison is obtained with five iterations on the NQC amplitude parameters (a_1^{22}, a_2^{22}), which correct the $\ell = m = 2$ waveform, in order to determine them self-consistently, and not using the fits of Ref. [14] that were obtained with a different expression for $a_6^c(\nu)$. To ease the discussion here, we refer the reader to Sec. II of Ref. [14] for the definition and implementation of NQC corrections in TEOBResumS.

As additional evaluation of the quality of the EOB waveform, we compute the EOB/NR unfaithfulness. Given two waveforms (h_1, h_2), the unfaithfulness is a function of the total mass M of the binary and it is defined as

TABLE II. Table listing the main features of the various, nonspinning, quasicircular models developed throughout this paper.

				$a_c^6 = n_0(1+n_1\nu+n_2\nu^2+n_3\nu^3+n_4\nu^4)/(1+d_1\nu)$					
Model	D	Q	NQC iteration	n_0	n_1	n_2	n_3	n_4	d_1
D3Q3_NQC	3PN, $P_3^0[D]$	3PN	✓	46.5524	−24.2516	120.9594	−167.2242	⋯	−3.3998
D5Q5_NQC	5PN, $P_2^3[D]$	5PN	✓	104.6595	−23.2539	113.8091	−261.8068	⋯	3.6511
D5Q5	5PN, $P_2^3[D]$	5PN	✗	331.1899	−27.9217	268.4658	−1138.1009	1784.4727	0.063909
D3Q3	3PN, $P_3^0[D]$	3PN	✗	41.803	−24.5764	251.4175	−926.6667	1080.9227	0.71904
D5Q3	5PN, $P_2^3[D]$	3PN	✗	−42.0938	−28.8863	332.9101	−1494.0405	2275.5579	−2.3295

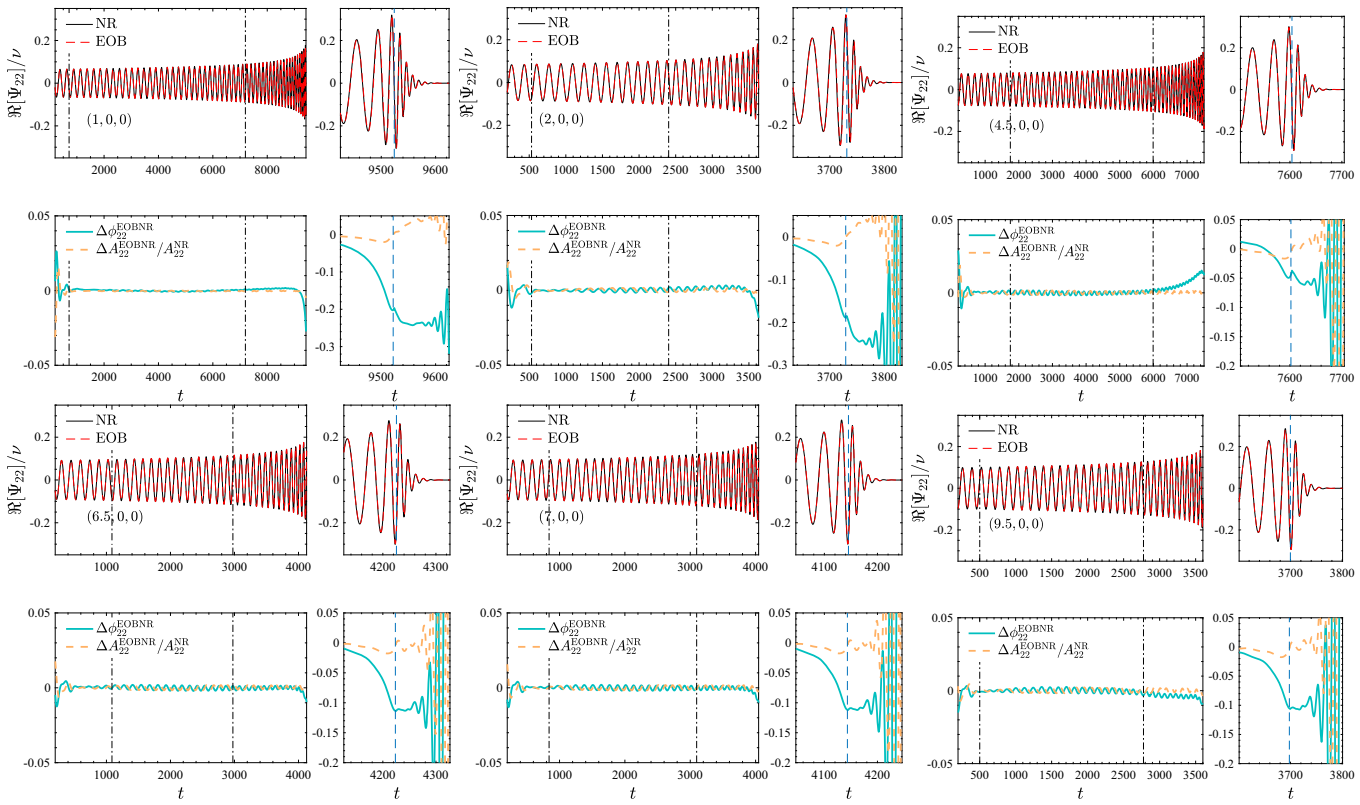

FIG. 1. `D3Q3_NQC` model: EOB/NR phasing agreement obtained with the new fit for a_6^c for the mass ratios $q = \{1, 2, 4.5, 6.5, 7, 9.5\}$ of Table I. Differently from previous work, a_6^c is tuned so that $\Delta\phi_{22}^{\rm EOBNR}$ decreases monotonically through merger and ringdown. Note how visible are the modulations due to residual NR eccentricity as the mass ratio is increased.

$$\bar{\mathcal{F}}(M) \equiv 1 - \mathcal{F} = 1 - \max_{t_0,\phi_0} \frac{\langle h_1, h_2\rangle}{||h_1||||h_2||}, \tag{3}$$

where (t_0, ϕ_0) are the initial time and phase. We used $||h|| \equiv \sqrt{\langle h, h\rangle}$, and the inner product between two waveforms is defined as $\langle h_1, h_2\rangle \equiv 4\Re \int_{f_{\rm min}^{\rm NR}(M)}^{\infty} \tilde{h}_1(f) \times \tilde{h}_2^*(f)/S_n(f) df$, where $\tilde{h}(f)$ denotes the Fourier transform of $h(t)$, $S_n(f)$ is the detector power spectral density (PSD), and $f_{\rm min}^{\rm NR}(M) = \hat{f}_{\rm min}^{\rm NR}/M$ is the initial frequency of the NR waveform at highest resolution, i.e. the frequency measured after the junk-radiation initial transient. For S_n, in our comparisons we use either the zero-detuned, high-power noise spectral density of Advanced LIGO [56] or the predicted sensitivity of Einstein Telescope [31,32] and Cosmic Explorer [33]. Waveforms are tapered in the time domain to reduce high-frequency oscillations in the corresponding Fourier transforms. The computation is done over a sample of nonspinning SXS simulations with mass ratio ranging from 1 to 9.5, and the EOB/NR unfaithfulness is then denoted as $\bar{\mathcal{F}}_{\rm EOB/NR}$.

The result of this computation is displayed in Fig. 2. For aLIGO, the largest values graze the 5×10^{-4} level, correspond to $q = 1$ and $q = 1.5$ and are somehow outliers with respect to the other configurations, where one easily gets to 2×10^{-4}. Inspecting the time-domain phasings of Fig. 1, one understands that this is the effect of lowering the phase difference at merger from $\Delta\phi_{22}^{\rm EOBNR} \equiv \phi_{22}^{\rm EOB} - \phi_{22}^{\rm NR} \sim 0.2$ rad to $\Delta\phi_{22}^{\rm EOBNR} \sim 0.1$ rad (see e.g. the $q = 9.5$ case). Changing to Einstein Telescope in its D configuration (ET-D) and Cosmic Explorer (CE) the worst values of $\bar{\mathcal{F}}_{\rm EOB/NR}$ are largely unchanged, with all datasets clustering around 10^{-4}. It thus seems that obtaining a model that is *more* NR faithful (i.e. at the 10^{-5} level or below) mostly amounts at *further reducing* the phase difference around merger. By contrast, an imperfect control of $\Delta\phi_{22}^{\rm EOBNR}$ around merger yields an important reduction of the EOB/NR agreement.

The reader should now be reminded that we stated that a_6^c was carefully chosen such that the phase difference $\Delta\phi_{22}^{\rm EOBNR}$ is small and decreases monotonically, mentioning this as an essential qualitative feature to be controlled in the NR-information process of a_6^c. Our statement can be understood by inspecting Fig. 3. The top panel of the figure compares two EOB/NR phase differences for $q = 1$: one obtained with the standard value of a_6^c of `TEOBResumS` (that is $a_6^c \simeq -41.16$) and the other with the improved value obtained above $a_6^c \simeq -35.93$. We see that in the former case the phase difference, which is not monotonic around merger, yields $\bar{\mathcal{F}}_{\rm EOB/NR}$ 2 times larger than in the optimized case.

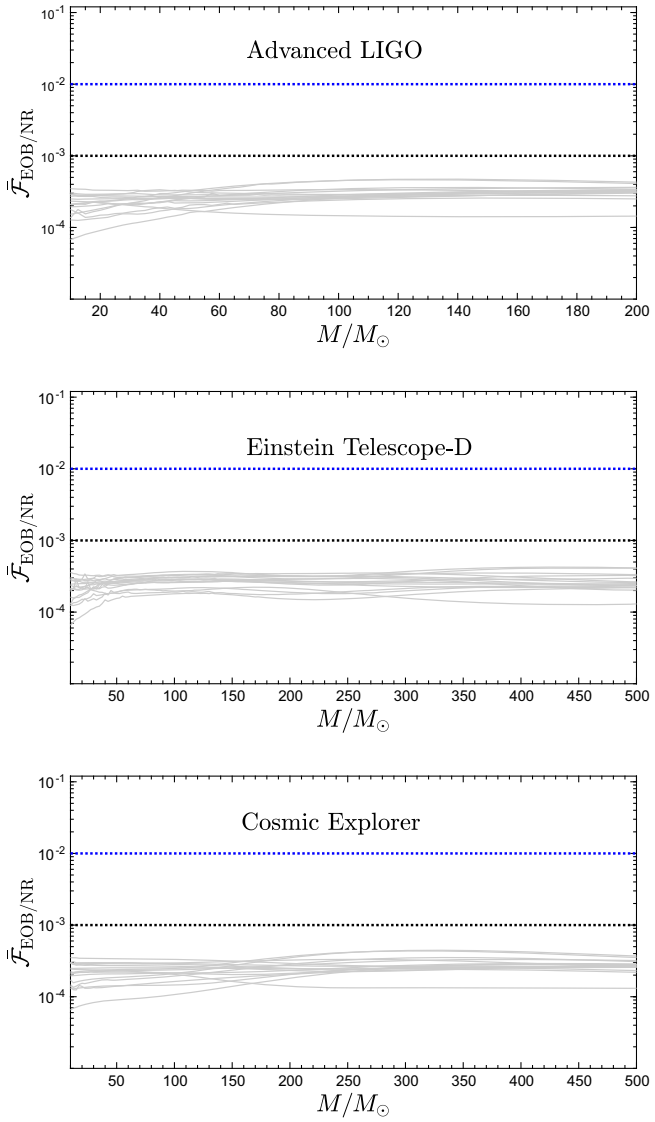

FIG. 2. EOB/NR unfaithfulness over all SXS nonspinning datasets listed of Table I. The top panel is obtained using the Advanced LIGO PSD, the central panel uses the ET-D configuration for the Einstein Telescope (see also Fig. 11 of Ref. [57]), and the bottom panel uses the expected PSD for Cosmic Explorer. The dotted blue and black lines mark respectively the 3% and 1% thresholds.

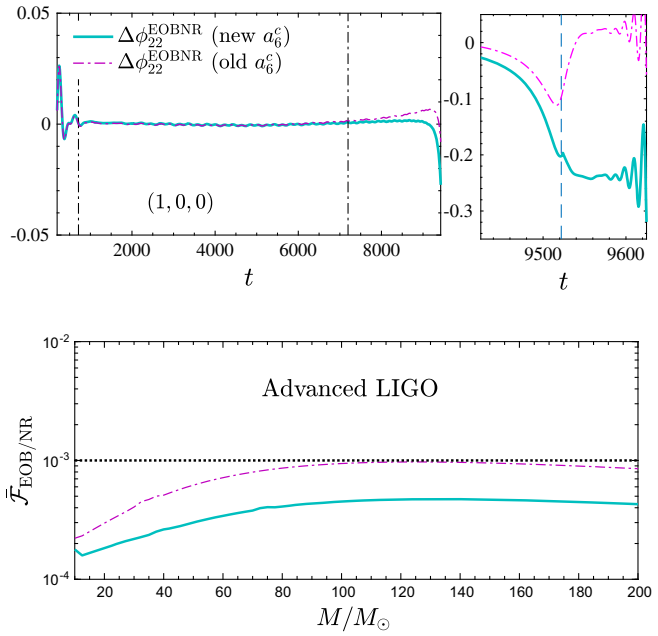

FIG. 3. Effect of small changes in a_6^c for $q = 1$. The old value is $a_6^c \simeq -41.16$, the standard TEOBResumS one, while the new one is $a_6^c \simeq -35.93$. The figure highlights the relation between the monotonically decreasing $\Delta\phi_{22}^{\rm EOBNR}$ and the unfaithfulness. A value of a_6^c that is suboptimal corresponds to approximately a loss of 5×10^{-4} in unfaithfulness.

In conclusion, this understanding allows to put on a solid basis what is additionally required to further improve the model: one needs to *flatten* the phase difference further through merger ringdown. This can be achieved by experimenting with the analytic content of the model, notably the nonradial pieces of the dynamics or augmenting the importance of NR data through merger and ringdown. Some of these effects will be investigated in the next section. Let us however mention, in passing, that an important improvement may come from a different determination of the NR-informed NQC correction to the phase. The procedure currently implemented in the model is still the one outlined in Ref. [37] (see Sec. III D therein) and might need to be revised or updated, e.g. with an additional NQC phase parameter determined by imposing continuity between the EOB and NR third derivative of the frequency. To do this properly, dedicated studies in the test-particle limit are currently ongoing [58], and we do not pursue this investigation further here but limit ourselves to mention it.

III. ANALYTIC SYSTEMATICS

In this section we attempt a preliminary investigation of what we call *analytic systematics*. By this term we address features of the EOB waveforms that depend on specific choices of analytic elements entering the model. A rather naive way of thinking about analytic systematics is within post-Newtonian (PN) theory, assuming that they arise from the lack of higher PN orders and studying the impact of such missing terms on the waveform generation [4]. This approach, while useful to test the sensitivity of parameter estimation to some "small" modifications of a model, is rather misleading because of the well-known asymptotic, nonconverging nature of PN series in strong field, exactly where such high order terms are expected to become most relevant. Indeed, in place of simple PN expansions, it is desirable to use resummed analytical expressions [59], even for the description of inspiral waveforms. In light of this fact, the EOB approach—with all its different avatars—represents the most natural formalism to *quantitatively*

study this kind of systematic effects, given its robustness and reliability also in the strong field regime.

There are many elements of EOB-based models that can be affected by systematics. To quote a few: (i) the PN truncation of the EOB potentials (A, D, Q), their resummed expressions and their NR-completion (preliminary explored in Refs. [12,19,34,52,60]); (ii) the PN truncation and resummation of the angular momentum flux, that impacts the radiation reaction and becomes more and more important for long inspirals and large mass ratios [61–65]; and (iii) the way NR information is incorporated in the model. Below we focus on two analytic systematics: (i) the importance of the time where the inspiral-to-plunge EOB waveform is attached to an analytic description of the ringdown and (ii) the importance of terms beyond 3PN in the EOB potentials (D, Q), and their link to NQC parameters.

A. The role of the matching point

So far, we have seen that it is relatively easy to improve the performance of the state-of-the-art TEOBResumS model simply by introducing slight changes in the way the single EOB-flexibility function $a_6^c(\nu)$ is determined. This yields EOB/NR unfaithfulness values that are at most $\sim 5 \times 10^{-4}$, with a gain of a factor 2 in the worst cases with respect to the previous model. This value is still larger than, though compatible with, the nominal NR uncertainty and reflects a phase difference at merger that is of order ~ 0.2 rad. As such, one is expecting that the EOB/NR agreement can be improved further. In this respect, we remind the reader that we are NR informing a *single* free parametric function, while the SEOBNR lineage of models [35,66,67] uses *two* for the same setup (nonspinning black hole binaries) to obtain comparable results (see [35]). More specifically, the SEOBNR family NR calibrates: (i) the analogous of a_6^c, a function called K (or even a_6^c in the latest SEOBNRv5 model [35]), and (ii) the temporal location of the peak of the $\ell = m = 2$ waveform. Within TEOBResumS the analogous of this second parameter is called $\Delta t_{\rm NQC}$, which is defined as follows. Calling $\Omega_{\rm orb}$ the orbital frequency[4] and $t_{\Omega_{\rm orb}^{\rm peak}}$ the time when it peaks, the interval $\Delta t_{\rm NQC}$ identifies on the EOB time axis the time $t_{\rm NQC}$, where we compute the NQC corrections,

$$t_{\rm NQC}^{\rm EOB} = t_{\Omega_{\rm orb}}^{\rm peak} - \Delta t_{\rm NQC}, \tag{4}$$

by imposing there that the EOB waveform (amplitude, phase and their time derivatives) coincides with the NR one, the latter evaluated $2M$ after the NR merger. See in particular Refs. [68,70] for the technical details of the procedure. Following Ref. [70], we have that

$$\Delta t_{\rm NQC} = 1. \tag{5}$$

This choice is motivated by the fact that, in the test-mass limit, this separation is $\lesssim 1$. More precisely, for the case of a test-mass plunging on a nonspinning black hole, one finds that $\Delta t_{\rm NQC} = 0.56$ (see Table 3 of[5] Ref. [69]). Analogously, for a test-particle plunging on a *spinning* black hole, we have that $\Delta t_{\rm NQC} \lesssim 1$ and it grows as the black hole spin increases. See in particular Table A 3 of Ref. [69]. On the basis of this test-mass knowledge, the condition of Eq. (5) was considered as a good, and simple, compromise and we did not attempt to inform *also* this parameter using NR simulations, although *a priori* one is expecting it to depend on *both* the mass ratio and the spins. It is thus interesting to explore to which extent an additional tuning of $\Delta t_{\rm NQC}$ can impact the model performance. To do so, we focus on the $q = 1$ case, which is the one showing the largest disagreement with the NR waveform. The top panel of Fig. 4 compares three phase differences $\Delta\phi_{22}^{\rm EOBNR}$: (i) the standard one, with $\Delta t_{\rm NQC} = 1$ and $a_6^c \simeq 35.93$; (ii) the one obtained using $\Delta t_{\rm NQC} = -0.8$ but keeping a_6^c unchanged (magenta, dash-dotted line); and (iii) the one with $\Delta t_{\rm NQC} = -0.8$ and $a_6^c = -55$, i.e. after an additional tuning of this parameter. Interestingly, one gains about a factor 2 around merger, although some $+0.02$ rad are now lost during the late inspiral. The bottom panel of the figure quantifies this information in terms of EOB/NR unfaithfulness: to a gain of about 2×10^{-4} for high masses corresponds to a loss of $\sim 1 \times 10^{-4}$ for low masses. This analysis evidences that the tuning of $\Delta t_{\rm NQC}$ could actually be helpful in improving the EOB/NR phase agreement around merger. However, the slight loss during the late inspiral seems to suggest it is not the best way of proceeding and alternative routes should probably be explored. Moreover, it requires an additional complication (tuning two parameters with NR data instead of one) that should possibly be faced only *after* other analytic elements are carefully considered and evaluated. It is certainly not impossible to NR tune two parameters at the same time,

[4]In the presence of spin, this is replaced by the *pure* orbital frequency, $\Omega_{\rm orb} = \partial_{p_\varphi} \hat{H}_{\rm orb}$, i.e. the orbital frequency without the contribution coming from the spin-orbit Hamiltonian, see [68]. The use of this function was inspired by features in the test-mass limit [68,69] that indicate that the peak of the quadrupolar waveform is always close to the peak of $\Omega_{\rm orb}$ [69] for values of the spin compatible to those of the final black hole that can be generated from BBH coalescences. As such, it is the pivotal element of the TEOBResumS construction, since it offers a natural, and simple, anchor point to define the merger time. Note in addition that $\Omega_{\rm orb}$ always has a maximum, differently from the complete orbital frequency Ω, whose structure depends on subtle interplays between the (necessarily approximated) descriptions of the orbital and spin-orbit sector of the Hamiltonian.

[5]Actually, the value is 0.38 or 0.56 depending whether it is calculated using Teukode or by solving directly the Regge-Wheeler-Zerilli equations with an hyperboloidal layer [71,72].

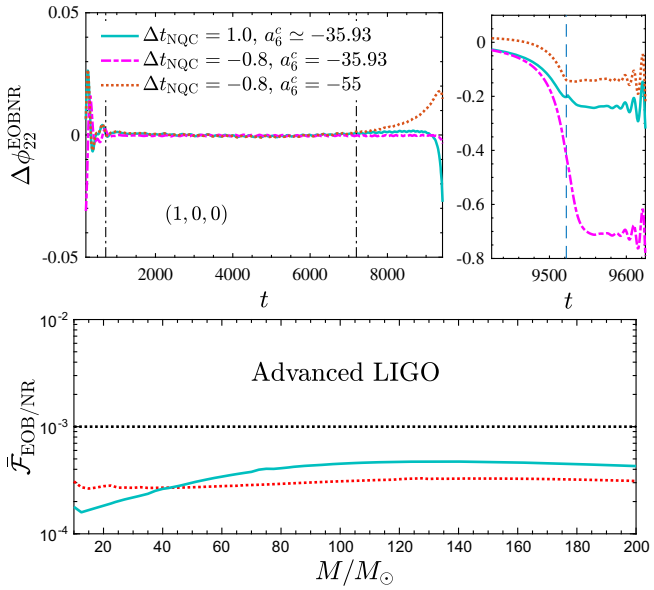

FIG. 4. Equal-mass case: effect of tuning, at the same time, a_6^c and $\Delta t_{\rm NQC}$. An improvement around merger ringdown seems to be balanced by a slight worsening during the late inspiral. This is apparent also looking at the EOB/NR unfaithfulness.

and indeed this is currently done for EOB models of the SEOBNR family [35,66,67]. However, since TEOBResumS allows for a simple and efficient iterative tuning of a_6^c only that yields highly accurate waveforms, we believe that this complication should be currently avoided. Possibly, it should be implemented *only after* a new analysis of the structure of the merger in the test-mass limit and its connection to the comparable-mass case is performed. In this respect, a seminal study was performed in Ref. [55], see Sec. IV B therein. An update of that analysis with the current, more accurate, SXS waveforms is in order and will be considered in future work.

B. D and Q up to 5PN accuracy

Let us now analyze in detail the other obvious source of analytic systematics, namely the PN accuracy of the EOB potentials. The impact of currently known analytical information at high PN order (notably, up to 6PN) was partially explored in Refs. [12,34]. In particular, in the context of constructing a spin-aligned EOB model for generic (nonquasicircular) planar orbits, Ref. [34] already explored the effect of the currently known analytical information at 5PN in (A, D, Q). To do so, in order to avoid the occurrence of spurious poles, the resummation of the A function was performed using a (3, 3) Padé approximant; similarly, D was resummed using a (3, 2) approximant, while the Q function was kept in PN expanded form. In addition, Ref. [34] also compared various Padé-based resummations for D, concluding that the (3, 2) is the best compromise at this PN order. Since the focus of [34] was on eccentric orbits (and scattering), the performance of the 5PN-accurate (D, Q) potentials was not explicitly spelled in the context of quasicircular binaries, i.e. using the standard quasicircular radiation reaction of TEOBResumS.

The aim of this section is to fill this gap in our knowledge by exploring how changes in (D, Q) affect the quasicircular model discussed above. We do so either by (i) following our standard approach of iterating on the NQC amplitude parameters (a_1, a_2) or (ii) removing the iteration, similar to the procedure followed for the eccentric model [34]. We will explore different PN truncations of (D, Q) and in each case we will determine a new $a_6^c(\nu)$ function, compute EOB/NR time-domain phasing and unfaithfulness. The properties of the nonspinning models we are going to compare and contrast are listed in Table II. Let us now analyze them one by one.

1. `D5Q5_NQC`: 5PN and iteration on NQC parameters

Let us start by considering a simple modification of TEOBResumS, dubbed `D5Q5_NQC`, where we replace D and Q at 3PN with their 5PN counterparts. The analytic expressions are precisely those of Eqs. (3) and (5) of Ref. [34]. In particular, for simplicity we use only the *local* part of Q and omit its nonlocal contributions. Similarly, in D we set to zero the analytically unknown coefficient $d_5^{\nu^2}$. The D function is then resummed with a (3, 2) Padé approximant. For each mass ratio considered, we determine the best a_6^c value inspecting the EOB/NR phasing and requiring, as in the previous case, that the phase difference possibly decreases monotonically through merger and ringdown. The corresponding values of a_6^c, shown in the top-left panel of Fig. 5, can be easily fitted with the same rational function given by Eq. (1) above. The fitting coefficients can be read from Table II. The corresponding EOB/NR time-domain phasings for $q = (1, 2, 4.5, 6.5, 9.5)$, obtained with the fitted a_6^c function, are shown in Fig. 5. From visual inspection, it is evident that the EOB/NR phasing agreement is less good than the one of Fig. 1, obtained using $D_{\rm 3PN}$ and $Q_{\rm 3PN}$. Note in particular that there is a non-negligible positive phase difference that accumulates *already* during the late inspiral up to merger and that cannot be absorbed by tuning a_6^c. This effect is more evident when q is small: for $q = 1$ one reaches $\Delta\phi_{22}^{\rm EOBNR} \sim 0.1$ at merger time, which then changes sign to reach -0.3 during the ringdown. The EOB performance degrades further for $q = 2$, although—for larger mass ratios—$\Delta\phi_{22}^{\rm EOBNR}$ is compatible with the corresponding cases of Fig. 1. The sign change of $\Delta\phi_{22}^{\rm EOBNR}$ around merger time negatively impacts on the unfaithfulness calculation, as illustrated in Fig. 5. The curves are generally more spread than in Fig. 2, with a few configurations [those with mass ratios $q = (1, 1.5)$] above the 0.1% level.

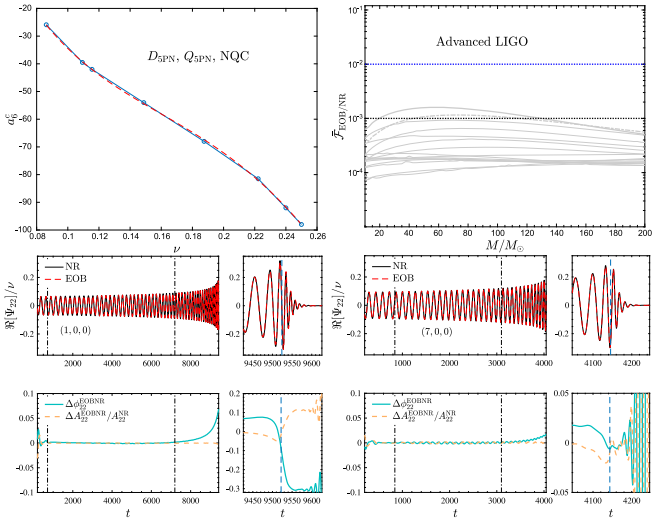

FIG. 5. D5Q5_NQC model: EOB/NR phasing analogous to Fig. 1, though using the complete, analytically known, 5PN information in (D, Q), with the D function resummed using a (3, 2) Padé approximant. Note that the phase difference accumulated already *before* merger for $q = 1$ is much larger than what occurs for D3Q3_NQC, Fig. 1.

This exercise demonstrates that it is possible to construct an EOB model, within a given EOB paradigm, that incorporates currently available 5PN information in the (D, Q) potentials, that is *less* NR faithful than an analogous model that only incorporates 3PN information in the same functions. This looks somehow counterintuitive. A commonly accepted statement within the gravitational wave modeling community is that the quality of the waveform model *improves* by increasing the order of the PN information used to construct it. As a consequence, high-PN results are usually considered an essential element to obtain highly faithful waveform models for current and future GW detectors. Our simple exercise demonstrates that this simple statement *may not always be* true, at least for the considered EOB potentials, as it depends on other features of the model. In particular, in an attempt to frame this statement in a wider context, in the next section we will explore what happens when the well-established practice of iterating on the amplitude NQC parameters (a_1, a_2) is removed.

2. D5Q5: 5PN and no iteration on NQC parameters

It is well known that NQC corrections are an essential element of EOB models. They were introduced long ago to correctly match the structure of the EOB waveform with the numerical one around merger [26,27,73]. In particular, Ref. [29] introduced the *iteration* on the NQC amplitude parameters, in order to accomplish consistency between the waveform and the flux. This proved important in several cases to get a high level of consistency between analytical and numerical data (see, e.g., Ref. [57] and references therein). However, as we will better understand at the end of this section, the iteration on (a_1, a_2) introduces an additional coupling between the conservative (i.e. the Hamiltonian) and the nonconservative (i.e. the radiation reaction) parts of the dynamics, so that the actual effect of each part is somehow hidden by this nonlinear, though extremely effective, procedure. To comply with the guiding philosophy of this paper, i.e. understanding the effect of each single theoretical element of the model, let us now *drop* the NQC iteration in order to get a clear understanding of the strong-field action of (D, Q). To start with, we focus on an equal-mass configuration and fix $a_6^c = 0$ for simplicity. In Fig. 6 we compare the EOB/NR phase difference $\Delta\phi_{22}^{\rm EOBNR} \equiv \phi_{22}^{\rm EOB} - \phi_{22}^{\rm NR}$ for three different choices of (D, Q): (i) the standard one of TEOBResumS (D_{3PN}, Q_{3PN}); (ii) the case (D_{5PN}, Q_{3PN}); and (iii) (D_{5PN}, Q_{5PN}). In terms of the dynamics, the figure shows that the plunge driven by the 3PN functions is *faster* than the NR one, so that a non-negligible, *positive*, phase difference builds up to merger (vertical dashed line in the right panel of Fig. 6). By contrast, the D_{5PN} function, resummed with (3, 2) Padé approximant, acts in the opposite direction, i.e. by *delaying the plunge* with respect to NR, so that $\Delta\phi_{22}^{\rm EOBNR} \sim -0.2$ rad at merger. When we consider also 5PN (local) terms in Q, the phase difference results almost flat throughout merger and ringdown. This finding seems to indicate that the iterative procedure for obtaining self-consistent NQC parameters (either in the waveform and in the flux), as introduced long ago [29], conflicts with high-order PN corrections in the D and Q potentials. To gain a deeper understanding on what is going on for D5Q5_NQC, in Fig. 7 we switch on the NQC iteration keeping $a_6^c = 0$ first for consistency with Fig. 6. One sees immediately that the NQC iteration is equivalent to a large repulsive effect in the dynamics, with the EOB merger delayed with respect to the NR one (vertical dashed line in the right panel of the figure), so that $\Delta\phi_{22}^{\rm EOBNR}$ is large and *negative*. The tuning of a_6^c allows one to partly *compensate* this effect, as the cases $a_6^c = -40$

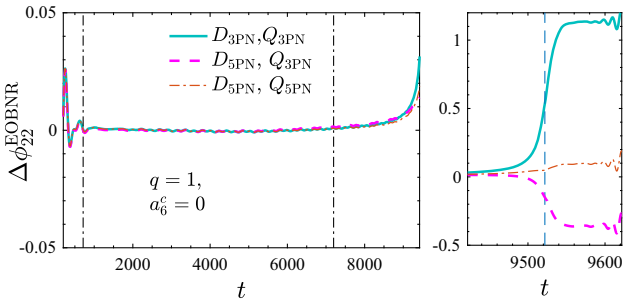

FIG. 6. EOB/NR phasing comparison for $q = 1$. Here we fix $a_6^c = 0$ and do not iterate on the NQC parameters (a_1, a_2). Increasing the amount of PN information in the D and Q functions seems to go in the good direction and improves the EOB/NR phasing agreement during the plunge up to merger. See text for discussion.

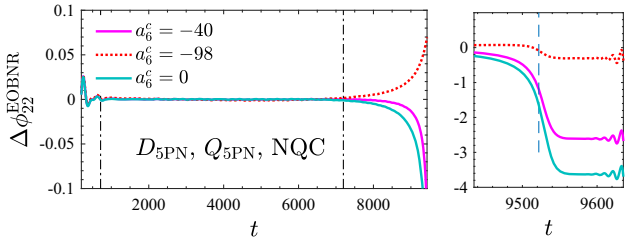

FIG. 7. Complement to Fig. 6. The iteration on the NQC parameters is equivalent to a *repulsive* effect in the potential, i.e. the merger gets strongly delayed. Note that the $a_6^c = 0$ line here is how the red dashed curve of Fig. 6 is modified due to the action of the iterated NQC. This feature can be *partly compensated* by tuning a_6^c, although the price to pay to have an acceptable phasing at merger is a progressive worsening of the phasing during the late inspiral (see line for $a_6^c = -98$, that is the value corresponding to `D5Q5_NQC`). This curve here corresponds to $\Delta\phi_{22}^{\mathrm{EOBNR}}$ in the bottom left panel of Fig. 5.

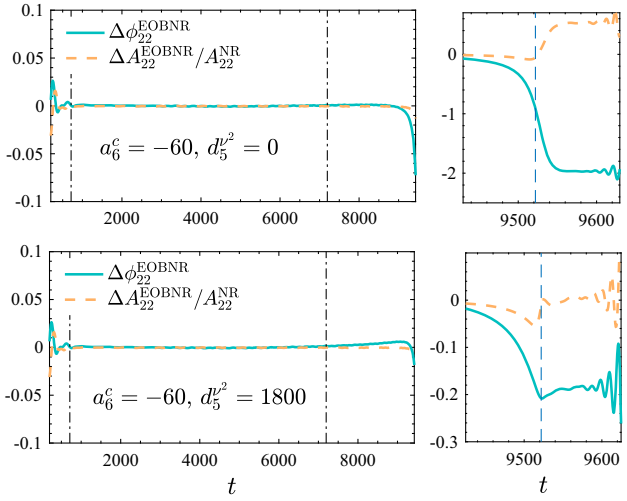

FIG. 8. Tuning in progression first a_6^c and then $d_5^{\nu^2}$ keeping the iteration on NQC parameters. The performance, for the $d_5^{\nu^2}$-tuned case, is visually comparable to `D3Q3_NQC` of Fig. 1.

and $a_6^c = -98$ in Fig. 6 illustrate. However, the price to pay to have an acceptable phasing at merger (such to yield $\bar{\mathcal{F}}^{\max}_{\mathrm{EOB/NR}} \lesssim 10^{-3}$) is a progressive worsening of the phasing during the late inspiral, as already pointed out in the above discussion on `D5Q5_NQC`. This suggests that, at least within the current analytic context, we are actually *overfitting* a_6^c (which belongs to the quasicircular regime) to fix some missing physical effects that belong to the genuine noncircular regime. The drawback of this overfitting is the loss of performance during the late inspiral. To overcome this difficulty, one could attempt to tune the noncircular potentials to further improve the behavior during plunge and merger *without* worsening the inspiral. The tuning on the noncircular dynamics could be implemented, for example, by tuning the currently unknown[6] residual 5PN coefficient $d_5^{\nu^2}$ in D. A successful attempt in this direction is shown in Fig. 8. In the top panel we tune iteratively a_6^c with the aim of reducing the phase difference at merger as much as possible keeping $\Delta\phi_{22}^{\mathrm{EOBNR}}$ negative and monotonically decreasing. The bottom panel shows that a rather large value of $d_5^{\nu^2}$ can actually reduce $\Delta\phi_{22}^{\mathrm{EOBNR}}$ during late plunge, merger and ringdown. Note that the phasing here, though still improvable, is substantially comparable to the top-left panel of Fig. 1. This exercise thus shows that *even* working with $(D_{5\mathrm{PN}}, Q_{5\mathrm{PN}})$ it is possible to use NQC corrections in a self-consistent way and obtain a highly accurate model, but one should NR inform both the circular and noncircular part of the dynamics.

Because of the level of additional complication of tuning two dynamical parameters at the same time, and given the already good performance of the model without NQC iterations for $q = 1$ and $a_6^c = 0$ seen above, it is then interesting to investigate the performance attainable using $(D_{5\mathrm{PN}}, Q_{5\mathrm{PN}})$ for nonspinning binaries *without* iterating on the NQC parameters (a_1, a_2). Now and below we will refer to this model as `D5Q5`. We thus perform a new determination of a_6^c versus ν using the usual procedure, as shown in the top left panel of Fig. 9. The ν dependence is more complicated than the previous cases, especially because the curve becomes rather steep as $\nu \to 0.25$. This entails that one would need more NR simulations in the range $0.2 \lesssim \nu \lesssim 0.25$ to correctly determine the shape of the curve. For consistency with our previous result, we add a few more datasets, but not many, and we limit ourselves to those where the initial values of the dimensionless spins are below 10^{-4} to avoid contamination from the small spins. An accurate representation of the points is given by a (4, 1) rational function in ν, with the coefficients that can be read off Table II. This gives a representation of the current data that is good enough, although certainly suboptimal to what is attainable using more NR simulations. The EOB/NR unfaithfulness for the usual nonspinning configurations is shown in the right panel of Fig. 9. At first sight, the performance is globally compatible to the standard result of Fig. 2, so that it seems that no special gain is found. However, looking at $\bar{\mathcal{F}}^{\max}_{\mathrm{EOB/NR}}$ (top right panel of Fig. 9), one discovers that `D5Q5` performs *better* than `D3Q3_NQC` either for small or large values of q. This is further highlighted by the plots in the bottom row of Fig. 9, where the phasing improvement for $q = 9.5$ with respect to `D3Q3_NQC` is evident.

3. `D3Q3` and `D5Q3`: Varying D with no NQC

To complete the findings of the previous section, let us also explore the performance of TEOBResumS with Q fixed at 3PN order, *without* the iteration on NQC parameters and

[6]See however Ref. [74] for a recent complete calculation of the 5PN dynamics.

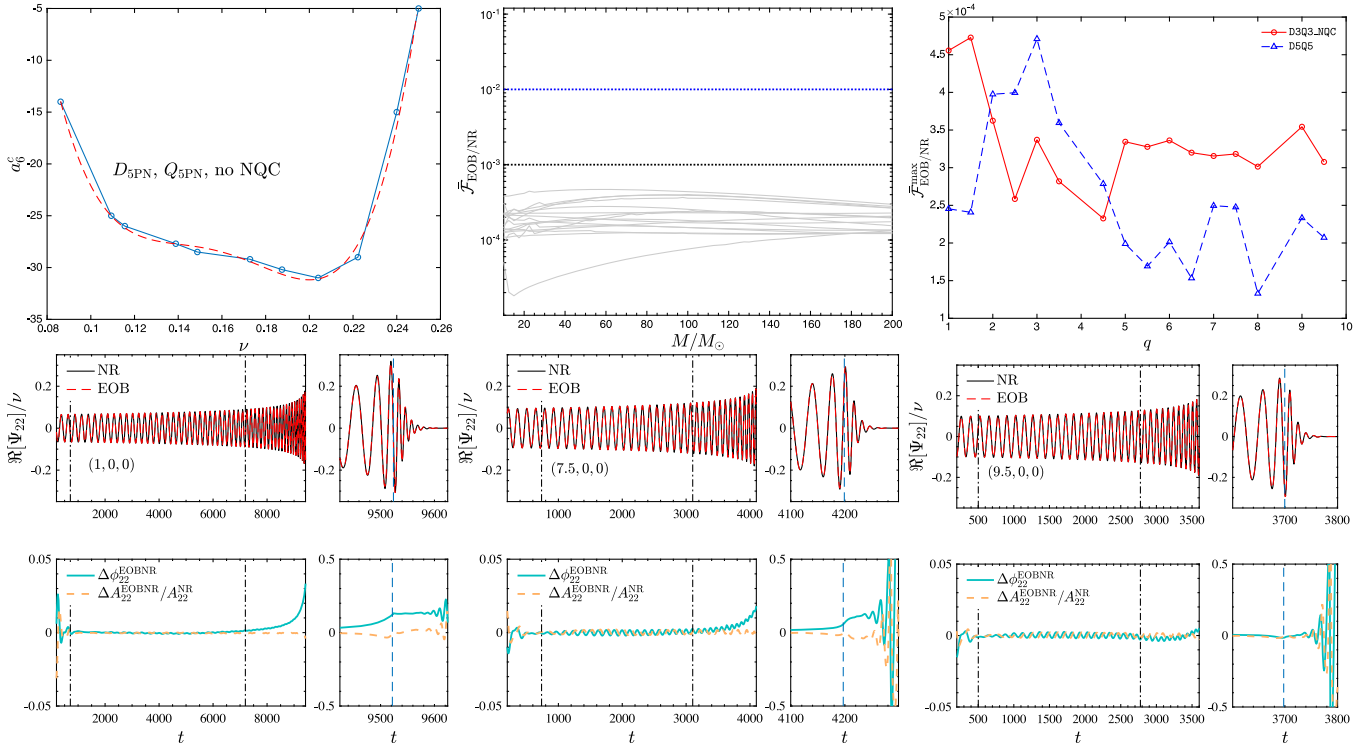

FIG. 9. D5Q5: performance of the model with (D_{5PN}, Q_{5PN}) and no iterations on the NQC amplitude parameters (a_1, a_2), see Table II. Top row: the left panel shows the NR-informed a_6^c, the middle $\bar{\mathcal{F}}_{EOB/NR}(M)$, and right one compares the corresponding $\bar{\mathcal{F}}^{max}_{EOB/NR}$ with that of D3Q3_NQC. A few illustrative time-domain phasings are also reported in the bottom row.

varying D. To start, we fix (D_{3PN}, Q_{3PN}) with D resummed with a (0, 3) Padé approximant, while A is resummed with the (1, 5) one and a_6^c is informed in the usual way using NR simulations. This model is simply dubbed D3Q3, see Table II. We find that the absence of the NQC correction in the radiation reaction (and thus the absence of the related repulsive effect discussed above) reduces the flexibility and accuracy of the model. As in the main text, a good fit of a_6^c is given by a (4, 1) rational function (see Table II). The fitted points and the fitting functions are shown in the top left panel of Fig. 10. The corresponding EOB/NR unfaithfulness, with the usual nonspinning datasets used above, on the Advanced LIGO PSD is shown in the top-right panel of Fig. 10, while the bottom panels show two time-domain phasings for two illustrative configurations. Interestingly, the largest EOB/NR phase differences (up to ∼1 rad) build up only during the last part of the plunge up to merger. It is useful to compare these plots with the corresponding panels in Fig. 1, which are obtained using the iterated NQC corrections in the flux. The phasing plots indicate how the NQC flux corrections, with their intrinsic repulsive character in strong field, are crucial to improve the dynamics *especially* through the late plunge up to merger, thus playing an essential role to achieve EOB/NR values of $\bar{\mathcal{F}}_{EOB/NR}$ *below* 10^{-3} found for D3Q3_NQC. In addition, thanks to the NQC iteration, the NR-informed a_6^c, which is

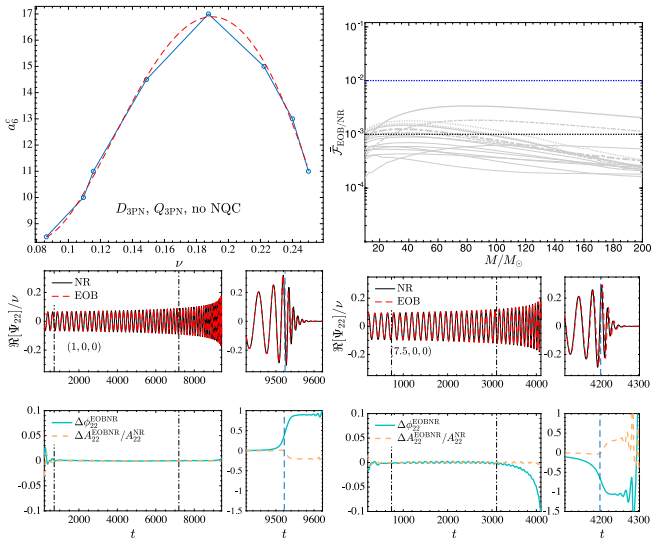

FIG. 10. D3Q3: performance of the model with (D_{3PN}, Q_{3PN}) and no NQC iteration. From left to right, top to bottom: the behavior of $a_6^c(\nu)$, $\bar{\mathcal{F}}_{EOB/NR}$ and two illustrative time-domain phasings. Note that the phase difference is positive and is accumulated only during the last orbit. Consistently with Fig. 7, and the effective repulsive effect due to the NQC iteration that here is missing, the EOB waveform is shorter than the NR one, with the plunge occurring earlier on.

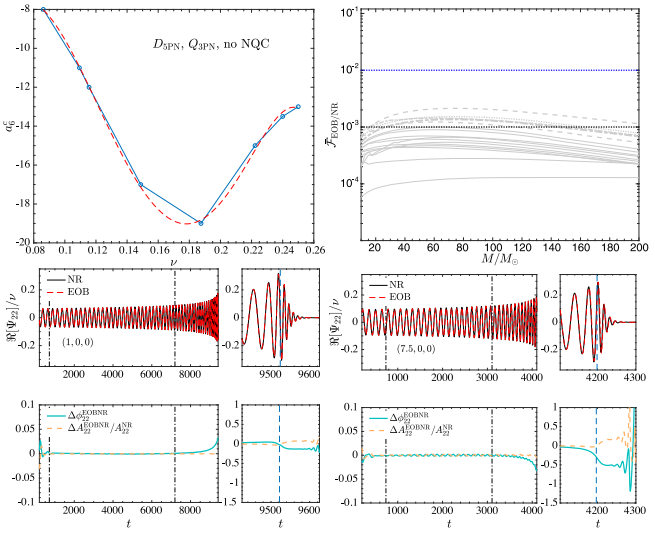

FIG. 11. D5Q3: model with (D_{5PN}, Q_{3PN}) and no NQC iteration. From left to right, top to bottom: the behavior of $a_6^c(\nu)$, $\bar{\mathcal{F}}_{EOB/NR}$ and two illustrative time-domain phasings. Note the improved performance with respect to the D3Q3 model shown in Fig. 10.

a priori expected to only affect the circular part of the dynamics, in practice propagates its action *also* on the noncircular part of the dynamics, allowing for a fine-tuning of the plunge-merger dynamics that is otherwise impossible.

To further support the importance of a the description of the radial part of the dynamics, Fig. 11 shows the performance of the model D5Q3, obtained with (D_{5PN}, Q_{3PN}). By comparing Figs. 10 and 11, it is apparent the improvement brought by moving from D_{3PN} to D_{5PN}, although the global performance is also influenced by the new determination of a_6^c.

IV. ECCENTRICITY AND SCATTERING

In Ref. [34] we developed an eccentric waveform model relying on the same (D_{5PN}, Q_{5PN}) functions discussed above, but with an A function resummed with a (3, 3) Padé approximant. In addition, the model of Ref. [34] was including explicit noncircular effects in radiation reaction (at leading Newtonian order) and in the waveform (including up to 2PN corrections [75–77]), both in factorized (and possibly resummed) form. In particular, the state-of-the-art TEOBResumS eccentric model now incorporates the new waveform introduced in Ref. [77] that relies on the direct differentiation of the quadrupole moment without explicit replacement of the 2PN-accurate equations of motion. As discussed in Ref. [77] this yields improved accuracy and robustness with respect to previous approaches [75,76]. Given our detailed analysis of the circular model of the previous section, it is then interesting to compare the performance of the quasicircular limit of the eccentric model. To do so, we do not precisely use the model of Refs. [34,76], but a version that is improved in three directions: (i) postadiabatic initial conditions, valid in the eccentric case, which continuously reduce to the postadiabatic conditions in the circular limit. This is important to avoid systematics in going to the circular limit of TEOBResumS that were recently pointed out [78]; (ii) a new expression of the radial force $\mathcal{F}_{r_*}$ where the quasicircular part is explicitly factorized, as proposed in Ref. [79]; and (iii) we find it unnecessary to use NR-informed NQC corrections to the waveform phase. Among these features, let us only note that the change of the radiation reaction is motivated by the fact that the $\mathcal{F}_{r_*}$ used in Ref. [34] is the main reason why the model is less NR faithful (see Fig. 8 of Ref. [34]) than the native quasicircular model for $q \sim 1$. As we will see below, this feature disappears once the following, circular-factorized, radial force is used:

$$\mathcal{F}_{r_*} = -\frac{5}{3}\frac{p_{r_*}}{p_\varphi}\mathcal{F}_\varphi \hat{f}_{p_{r_*}}, \tag{6}$$

where $\hat{f}_{p_{r_*}}$ is a quadratic function in u that reads

$$\hat{f}_{p_{r_*}} = 1 + \left(\frac{5317}{1680} - \frac{227}{140}\nu\right)u + \left(\frac{1296935}{1016064} - \frac{274793}{70560}\nu + \frac{753}{560}\nu^2\right)u^2, \tag{7}$$

which is then resummed using a (0, 2) Padé approximant. The corresponding best a_6^c values are fitted by the function

$$a_6^c = 175.5440\nu^3 + 487.6862\nu^2 - 471.7141\nu + 0.8178, \tag{8}$$

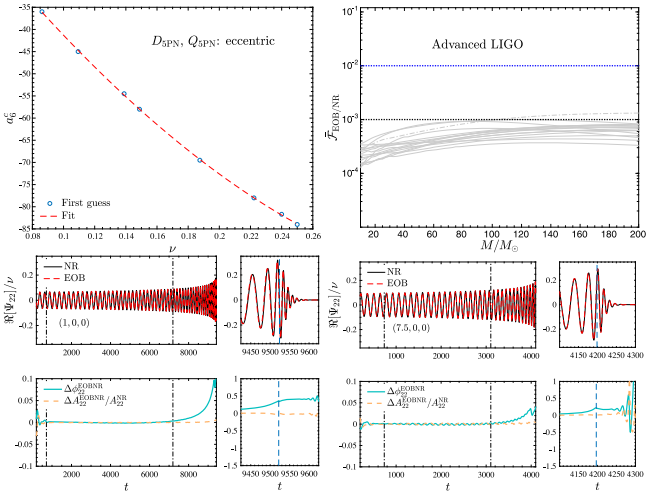

FIG. 12. Eccentricity: quasicircular limit of the eccentric nonspinning model. The EOB/NR performance is comparable to the improved TEOBResumS quasicircular model (with NQC iterations), and slightly better than the eccentric model of Ref. [34] for $q \approx 1$.

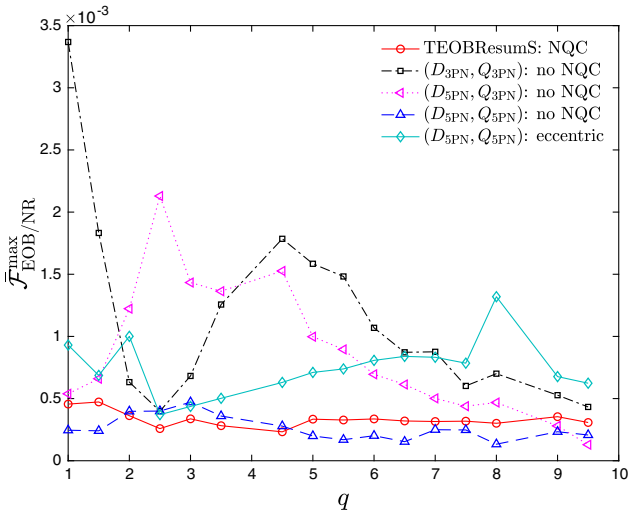

FIG. 13. The values of $\bar{\mathcal{F}}^{\max}_{\rm EOB/NR}$ for the quasicircular limit of the generic, noncircular (eccentric) model discussed in this section compared with the corresponding values obtained with quasicircular models discussed in Sec. III.

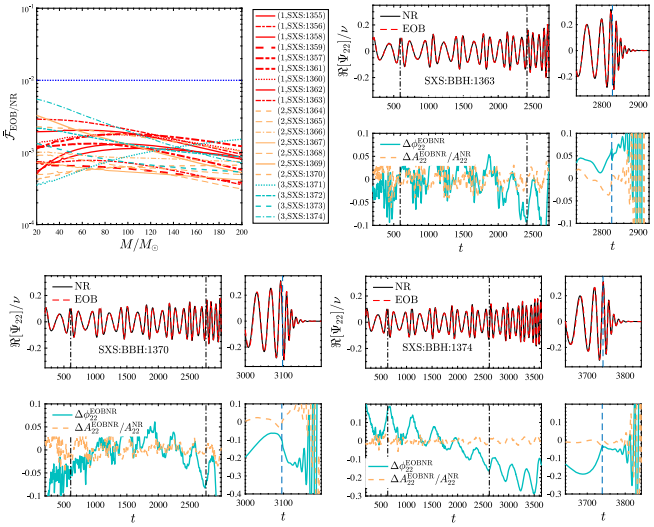

FIG. 14. Eccentricity: EOB/NR comparison for nonspinning configurations with different initial eccentricities. Top left panel: EOB/NR unfaithfulness. Other panels: time-domain phasing plots for the most eccentric configurations.

which is shown in the top-left panel of Fig. 12. Note that, although the values of a_6^c are slightly different from the best ones determined in Ref. [34], the qualitative shape of the function remains unchanged. The top-right panel of Fig. 12 shows the EOB/NR unfaithfulness, while the bottom panel the time-domain phasings for two illustrative configurations. We see that the performance of the quasicircular limit of the model is more than acceptable, though about 1 order of magnitude less good than the native quasicircular model with the same analytic choices for (A, D, Q) (see the top-middle panel of Fig. 9 as well as Fig. 13, where we compare $\bar{\mathcal{F}}^{\max}_{\rm EOB/NR}$ for all noncircular nonspinning models considered so far). Note that $\bar{\mathcal{F}}^{\max}_{\rm EOB/NR} \sim 0.1\%$ (also when $q = 1$) which shows an improvement by a factor 2 with respect to Ref. [34] (see Fig. 8 therein) due to the different choice of $\mathcal{F}_{r_*}$. When moving to eccentric configurations (on bound orbits) we perform the same kind of comparisons with the available SXS datasets discussed in previous works [34,80]. The various modifications we have introduced to the model call for small modifications to the initial EOB eccentricity and frequency at periastron

TABLE III. Comparison between EOB and NR scattering angle. From left to right the columns report: the ordering number; the EOB impact parameter $r_{\rm min}$; the NR and EOB radiated energies, $(\Delta E^{\rm NR}/M, \Delta E^{\rm EOB}/M)$; the NR and EOB radiated angular momentum, $(\Delta J^{\rm NR}/M^2, \Delta J^{\rm EOB}/M^2)$; the NR and EOB scattering angles $(\chi^{\rm NR}, \chi^{\rm EOB})$ and their fractional difference $\hat{\Delta}\chi^{\rm NREOB} \equiv |\chi^{\rm NR} - \chi^{\rm EOB}|/\chi^{\rm NR}$.

No.	$r_{\rm min}$	$\Delta E^{\rm NR}/M$	$\Delta E^{\rm EOB}/M$	$\Delta J^{\rm NR}/M^2$	$\Delta J^{\rm EOB}/M^2$	$\chi^{\rm NR}$ [deg]	$\chi^{\rm EOB}$[deg]	$\hat{\Delta}\chi^{\rm NREOB}$[%]
1	3.43	0.01946(17)	0.018003	0.17007(89)	0.166250	305.8(2.6)	315.6022	3.20
2	3.76	0.01407(10)	0.012124	0.1380(14)	0.124784	253.0(1.4)	258.2949	2.09
3	4.06	0.010734(75)	0.008743	0.1164(14)	0.098849	222.9(1.7)	225.0784	0.98
4	4.86	0.005644(38)	0.004152	0.076920(80)	0.058812	172.0(1.4)	171.5614	0.25
5	5.35	0.003995(27)	0.002842	0.06163(53)	0.045379	152.0(1.3)	151.2741	0.48
6	6.50	0.001980(13)	0.001370	0.04022(53)	0.027736	120.7(1.5)	119.9820	0.59
7	7.60	0.0011337(90)	0.000789	0.029533(53)	0.019227	101.6(1.7)	101.0896	0.50
8	8.68	0.007108(77)	0.000505	0.02325(47)	0.014333	88.3(1.8)	87.9789	0.36
9	9.73	0.0004753(75)	0.000347	0.01914(76)	0.011213	78.4(1.8)	78.1769	0.28
10	10.79	0.0003338(77)	0.000251	0.0162(11)	0.009081	70.7(1.9)	70.4980	0.28
11	3.03	0.0281(11)	0.0291	0.2220(64)	0.2366	307.1316	337.6476	9.94
12	3.91	0.01194(27)	0.0101	0.1252(10)	0.1098	225.5430	229.8746	1.92
13	4.41	0.00793(34)	0.0062	0.09456(70)	0.0780	207.0259	207.4499	0.20
14	4.99	0.004925(30)	0.0038	0.069504(39)	0.0560	195.9340	194.5736	0.69
15	6.68	0.001625(16)	0.0013	0.034511(71)	0.0280	201.9091	200.1535	0.87

$(e^{\rm EOB}_{\omega_a}, \omega^{\rm EOB}_a)$. Once this is taken into account, we compute the EOB/NR unfaithfulness, which is shown in the top-left panel of Fig. 14. On this diagnostics, the performance is substantially equivalent to previous versions of the model. On the contrary, the time-domain phasings, shown for the most eccentric configurations of the set, show evidence of some improvement with respect to previous versions of the model, especially through merger and ringdown. As a last investigation, we obtain the scattering angle for the $q = 1$ *nonspinning* configurations whose corresponding NR values are computed in Refs. [81,82]. Also here one finds a small, though non-negligible, improvement for most of the configurations, see Table III. This is particularly evident for the configurations simulated in Ref. [82], which generally span a stronger field regime than those of Ref. [81]. In particular, configuration number 11 in Table III has a EOB/NR fractional difference ∼10%, which means a ∼2.6% improvement with respect to Ref. [82] (see Table II therein) that was relying on the EOB model of Ref. [34]. The table also lists the values of the NR and EOB radiated energy and angular momentum as well as the closest EOB separation reached, indicated as $r_{\rm min}$.

V. SPINNING CONFIGURATIONS: IMPROVING THE TEOBResumS MODEL

A. From TEOBResumSv4.1.4 to TEOBResumSv4.2.0

Now that we have understood the importance of the modelization of the noncircular part of the dynamics in the nonspinning case, let us move to considering spins in TEOBResumS. In particular, we want to evaluate how the quality of the D3Q3_NQC expression of $a^c_6(\nu)$ propagates on the spin sector of the model. To do so efficiently, we mostly use the *C* implementation of TEOBResumS complemented, for simplicity, by the fits for the NQC parameters[7] entering the radiation reaction presented in [14]. Figure 15 shows the EOB/NR unfaithfulness all over the full SXS catalog obtained with the N^{3}LO c_3 parameter of TEOBResumS but with different choices for a^c_6. The left panel of Fig. 15 is $\bar{\mathcal{F}}_{\rm EOB/NR}$ with the standard $a^c_6(\nu)$ of TEOBResumS, while the right panel the same quantity obtained with the D3Q3_NQC a^c_6. It is interesting to note that the improvement in the orbital sector are by themselves sufficient to reduce the number of outliers above the 2×10^{-3} level. Note however that little improvement is obtained, for example, for the (1.5, 0.95, 0.95) configuration, although it remains the only outlier above 0.5%. In any case, the global lowering of the EOB/NR unfaithfulness is non-negligible already up to $M = M_\odot \sim 100$, i.e. for the total mass range covered by most of the events detected so far by the LVK collaboration [83]. Evidently, the EOB/NR performance is expected to improve further by

[7]We have verified that the differences with the iterated model are practically negligible.

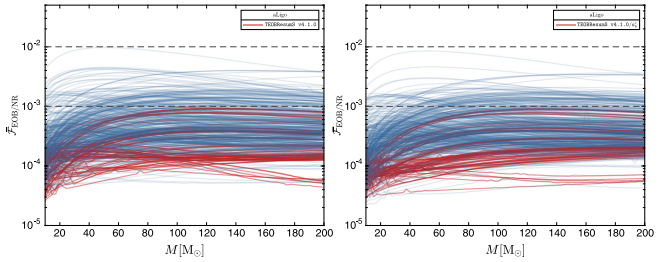

FIG. 15. EOB/NR unfaithfulness comparisons. Left panel: standard TEOBResumS. Right panel: improved model with the D3Q3_NQC $a^c_6(\nu)$ function of Table II but with the standard, NR-informed, N^{3}LO spin-orbit effective parameter c_3. The red curves correspond to all reliable nonspinning datasets. In this second case, the only outlier above 0.5% is $(1.5, +0.95, +0.95)$, SXS:BBH:1146.

a new determination of c_3 that is either more consistent with the current choice of a^c_6 or uses more NR data to better determine its dependence on the spins and mass ratio. In this respect, Ref. [57] introduced a new version of TEOBResumS that differs from the standard one because of: (i) more (NR-informed) NQC corrections in the flux, to achieve a closer EOB/NR flux consistency during the plunge phase up to merger and (ii) a different expression for c_3 obtained using a carefully chosen set of SXS NR simulations, see Table II in Ref. [57]. As a start, we can simply replace the standard TEOBResumS c_3 with the one given in Eq. (22) of Ref. [57] and explore whether the EOB/NR unfaithfulness is reduced. In general, the analytic expression of c_3 is made by two terms, one determined using only equal-mass and equal-spin configurations, $c_3^{=}$, and another one corresponding to all other combinations of mass ratios and spins, $c_3^{\neq}$. Globally, the c_3 function reads

$$c_3(\nu, \tilde{a}_0, \tilde{a}_{12}) = c_3^{=} + c_3^{\neq}, \tag{9}$$

where

$$c_3^{=} \equiv p_0 \frac{1 + n_1\tilde{a}_0 + n_2\tilde{a}_0^2 + n_3\tilde{a}_0^3 + n_4\tilde{a}_0^4}{1 + d_1\tilde{a}_0} \tag{10}$$

$$c_3^{\neq} \equiv (p_1\tilde{a}_0 + p_2\tilde{a}_0^2 + p_3\tilde{a}_0^3)\sqrt{1-4\nu} + p_4\tilde{a}_0\nu\sqrt{1-4\nu} + (p_5\tilde{a}_{12} + p_6\tilde{a}_{12}^2)\nu^2, \tag{11}$$

and $\tilde{a}_i \equiv X_i\chi_i$, $\tilde{a}_0 = \tilde{a}_1 + \tilde{a}_2$, and $\tilde{a}_{12} \equiv \tilde{a}_1 - \tilde{a}_2$, while (p_0, n_i, d_1, p_i) are fitting coefficients obtained by fitting the pointwise $c_3^{\rm first-guess}$ values obtained for a (possibly limited) number of NR configurations. The coefficients for the fit are found in the first row of Table IV, with the model dubbed TEOBResumSv4.2.0. Note that, following [57], we exactly impose $p_3 = p_6 = 0$. This constraint will be eventually relaxed below. Figure 16 illustrates that this expression of c_3 already brings a relevant improvement, so

TABLE IV. Coefficients for the fit of c_3 for models that share the same new determination of a_6^c but change mostly because of c_3. More precisely TEOBResumSv4.2.0 uses the c_3 function of Ref. [57]; TEOBResumSv4.3.0 shares the same $c_3^{=}$ but implements a new $c_3^{\neq}$ informed with NR datasets not used in Ref. [57] and all listed in Table; TEOBResumSv4.3.1 implements an improved representation of $c_3^{=}$ informed from the dataset of Table VIII that also yields a correspondingly updated $c_3^{\neq}$. As a last step TEOBResumSv4.3.2 implements a further modification of $c_3^{\neq}$ related to having changed the first-guess value for the SXS:BBH:1432 dataset from $c_3^{\text{first-guess}} = 25$ to $c_3^{\text{first-guess}} = 21$. Furthermore, this model also implements a different analytical representation of the NR NQC point used to determine (iteratively) the NQC corrections that is essential to remove the few outliers with unfaithfulness slightly above 0.2% always present for the other models.

	$c_3^{=} \equiv p_0(1+n_1\tilde{a}_0+n_2\tilde{a}_0^2+n_3\tilde{a}_0^3+n_4\tilde{a}_0^4)/(1+d_1\tilde{a}_0)$											
	$c_3^{\neq} \equiv (p_1\tilde{a}_0+p_2\tilde{a}_0^2+p_3\tilde{a}_0^3)\sqrt{1-4\nu}+p_4\tilde{a}_0\nu\sqrt{1-4\nu}+(p_5\tilde{a}_{12}+p_6\tilde{a}_{12}^2)\nu^2$											
Model	p_0	n_1	n_2	n_3	n_4	d_1	p_1	p_2	p_3	p_4	p_5	p_6
TEOBResumSv4.2.0	43.873	−1.849	1.0112	−0.0864	−0.0384	−0.888	26.553	−8.6584	0	−84.7473	24.0418	0
TEOBResumSv4.3.0	43.873	−1.849	1.0112	−0.0864	−0.0384	−0.888	16.6957	2.0250	−6.6009	−53.1461	34.0979	−101.0037
TEOBResumSv4.3.1	42.195	−2.0107	1.258	−0.1210	−0.1063	−0.9665	20.9956	1.5806	−10.428	−61.1980	37.1134	−37.6681
TEOBResumSv4.3.2	42.195	−2.0107	1.258	−0.1210	−0.1063	−0.9665	18.8003	0.6175	−10.398	−47.1696	33.4449	−32.5157

that TEOBResumS4.2.0 is closer to NR than its previous avatars. This is by itself remarkable considering that this c_3 was determined for a model with a different a_6^c and radiation reaction. One is left with only 11 outliers with $\bar{\mathcal{F}}^{\max}_{\text{EOB/NR}} > 0.2\%$ (listed in Table V) with the worst performance (0.42%) obtained for a $(3.64, +0.80, -0.43)$ configuration. From the table we see that most of the largest values are in the range $2 \lesssim q \lesssim 3$ and large values of the individual (unequal) spins. This is *a priori* not surprising considering that the c_3 above was determined using *only three* $q = 2$ and six $q = 3$ datasets, see Table II of Ref. [57], mostly equal-spin ones. On the one hand, this is a proof of the robustness of the analytic structure of TEOBResumS, as it can somehow automatically accommodate for the lack of additional NR information. On the other hand, it makes us *a priori* confident that a different determination of c_3 that relies on some more unequal-spin datasets should allow us to additionally lower $\bar{\mathcal{F}}^{\max}_{\text{EOB/NR}}$, possibly below 10^{-3} for all configurations.

B. From TEOBResumSv4.2.0 to TEOBResumSv4.3.2

Let us then embark into the enterprise of improving TEOBResumSv4.2.0 further. We anticipate that, by carefully understanding the origin of the EOB/NR (small) discrepancies, we will eventually succeed in obtaining a model, dubbed TEOBResumSv4.3.2, with $\bar{\mathcal{F}}^{\max}_{\text{EOBNR}} \sim 0.1\%$ all over the public SXS catalog. We note that this result will be achieved by *only* working on the NR-informed part of the model, without incorporating additional analytical information.

To start with, the simplest way to proceed seems to compute a new c_3 function by incorporating in the NR-informing data the ten outlier configurations of Table V.

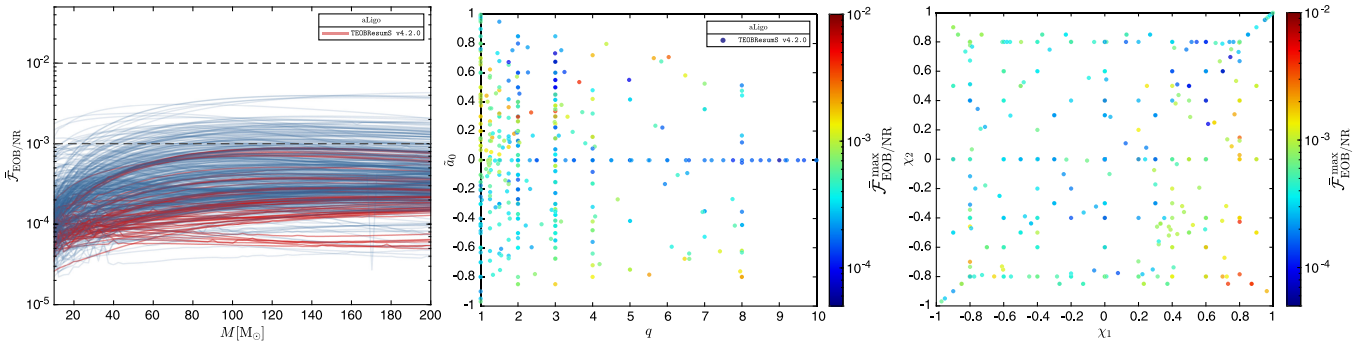

FIG. 16. Performance of TEOBResumSv4.2.0: the EOB/NR unfaithfulness over 534 datasets of the SXS catalog. The plot is obtained using the public implementation of the C TEOBResumS code where the native expression of a_6^c is replaced by the `D3Q3_NQC` one of Table II for a_6^c while c_3 is given by the first row of Table IV. Left panel: the EOB/NR unfaithfulness $\bar{\mathcal{F}}_{\text{EOB/NR}}$ versus the total mass of the binary. Middle: $\bar{\mathcal{F}}^{\max}_{\text{EOB/NR}}$ highlighting the dependence on q and $\tilde{a}_0$. Right panel: $\bar{\mathcal{F}}^{\max}_{\text{EOB/NR}}$ versus the dimensionless spins (χ_1, χ_2). One finds 11 configurations with $\bar{\mathcal{F}}^{\max}_{\text{EOB/NR}} > 0.2\%$, which are listed in Table V for convenience.

TABLE V. SXS datasets of Fig. 16 considered outliers, with $\bar{\mathcal{F}}^{\max}_{\rm EOB/NR} > 0.2\%$. Note that datasets SXS:BBH:0258 and SXS:BBH:2132 represent the same configuration.

No.	ID	(q,χ_1,χ_2)	$\bar{\mathcal{F}}^{\max}_{\rm EOB/NR}[\%]$
1	BBH:0552	(1.750100, +0.799926, −0.399972)	0.2126
2	BBH:1466	(1.896882, +0.698849, −0.799666)	0.2182
3	BBH:0258	(1.999666, +0.871258, −0.849486)	0.3899
4	BBH:2132	(1.999854, +0.871263, −0.849645)	0.3920
5	BBH:1453	(2.352106, +0.800164, −0.784292)	0.3684
6	BBH:0292	(2.999266, +0.731359, −0.849301)	0.3887
7	BBH:1452	(3.641386, +0.800138, −0.426550)	0.4252
8	BBH:1428	(5.516491, −0.800166, −0.699341)	0.2201
9	BBH:1440	(5.638278, +0.769754, +0.306334)	0.2094
10	BBH:1437	(6.037524, +0.799933, +0.147520)	0.3061
11	BBH:1419	(7.997128, −0.799957, −0.798880)	0.2364

TABLE VI. First-guess values for c_3 determined modifying the unequal-mass part. This gives the TEOBResumSv4.3.0 model whose performance is illustrated in Fig. 17.

#	ID	(q,χ_1,χ_2)	$\tilde{a}_0$	$c_3^{\rm first\ guess}$
15	BBH:0004	(1, −0.50, 0.0)	−0.25	55.5
16	BBH:0005	(1, +0.50, 0.0)	+0.25	35
17	BBH:2105	(1, +0.90, 0.0)	+0.45	27.7
18	BBH:2106	(1, +0.90, +0.50)	+0.70	19.1
19	BBH:0016	(1.5, −0.50, 0.0)	−0.30	56.2
20	BBH:1146	(1.5, +0.95, +0.95)	+0.95	14.35
21	BBH:0552*	(1.75, +0.80, −0.40)	+0.36	29
22	BBH:1466*	(1.90, +0.70, −0.80)	+0.18	33
23	BBH:2129	(2, +0.60, 0.0)	+0.40	29.5
24	BBH:0258*	(2, +0.87, −0.85)	+0.296	32
25	BBH:2130	(2, +0.60, +0.60)	+0.60	23
26	BBH:2131†	(2, +0.85, +0.85)	+0.85	15.8
27	BBH:1453*	(2.352, +0.80, −0.78)	+0.328	29
28	BBH:2139	(3, −0.50, −0.50)	−0.50	65.3
29	BBH:0036†	(3, −0.50, 0.0)	−0.38	61
30	BBH:0174	(3, +0.50, 0.0)	+0.37	28.5
31	BBH:2158	(3, +0.50, +0.50)	+0.50	27.1
32	BBH:2163	(3, +0.60, +0.60)	+0.60	24.3
33	BBH:0293†	(3, +0.85, +0.85)	+0.85	16.0
34	BBH:0292*	(3, +0.73, −0.85)	+0.335	30.6
35	BBH:1447	(3.16, +0.7398, +0.80)	+0.75	19.2
36	BBH:1452*	(3.641, +0.80, −0.43)	+0.534	25.6
37	BBH:2014	(4, +0.80, +0.40)	+0.72	21.5
38	BBH:1434	(4.37, +0.7977, +0.7959)	+0.80	19.8
39	BBH:0111	(5, −0.50, 0.0)	−0.42	54
40	BBH:0110†	(5, +0.50, 0.0)	+0.42	29.5
41	BBH:1428*	(5.516, −0.80, −0.70)	−0.784	80
42	BBH:1440*	(5.64, +0.77, +0.31)	+0.70	21.5
43	BBH:1432	(5.84, +0.6577, +0.793)	+0.68	25
44	BBH:1437*	(6.038, +0.80, +0.15)	+0.7076	21.5
45	BBH:1375†	(8, −0.90, 0.0)	−0.80	70
46	BBH:1419*	(8, −0.80, −0.80)	−0.80	81.5
47	BBH:0114†	(8, −0.50, 0.0)	−0.44	61
48	BBH:0065†	(8, +0.50, 0.0)	+0.44	26.5
49	BBH:1426	(8, +0.4838, +0.7484)	+0.51	30.3

Since these are all unequal-mass configurations, we will only update $c_3^{\neq}$. In following this procedure, we realized that it is useful to also update some of the first-guess values used in Ref. [57]. All datasets used to this aim are listed in Table VI. For the reader's convenience, we mark with an $*$ the *new* datasets (coming from Table V) added to inform c_3, while with a † the configurations that receive an updated value of $c_3^{\rm first-guess}$. The parameters of this new model, dubbed TEOBResumSv4.3.0, are listed in the second row of Table IV. The corresponding accuracy checks, versus NR, are exhibited in Fig. 17. The number of outliers above 2% is now reduced, with only three remaining configurations, listed in Table VII. However, from Fig. 17 we see that the performance is visibly lower for equal-mass binaries, and in particular in the range $0 \lesssim \tilde{a}_0 \lesssim 0.4$. This calls for an improved determination of $c_3^{=}$ in that spin range. To do so, we list in Table VIII the equal-mass, equal-spin configurations with the corresponding first-guess values. The table includes two datasets more than in Ref. [57] to constrain better the function for small, positive, spins. The corresponding new coefficients for *both* $c_3^{=}$ and $c_3^{\neq}$ are listed in the third row of Table IV, with the model now dubbed TEOBResumSv4.3.1. The performance is evaluated in Fig. 18. Globally, the number of dataset below 0.1% unfaithfulness is slightly larger than before. However, we find now *four* outliers above 0.2%, see Table IX. Notably, some are the same as Table V. These suggest that, whatever is incorrect in the EOB model in this special corner of the parameter space, it should not be related to the determination of c_3. We thus performed a more careful investigation of the waveform properties for a particular configuration, the SXS:BBH:0258 one. We concluded that the waveform inaccuracies effectively come from the determination of the NQC corrections to the waveform and *not* from the choice of c_3. Let us discuss this in some detail. We remind the reader that the determination of the NQC parameters $(a_1^{22}, a_2^{22}, b_1^{22}, b_2^{22})$ needs some representation of the NR amplitude and frequency (and first derivatives) $(A_{22}, \dot{A}_{22}, \omega_{22}, \dot{\omega}_{22})$ across the parameter space. More precisely, Ref. [36] represented these quantities via NR-informed fits, in the form discussed in Appendix C 5. By computing the waveform using the *exact* NR values of $(A_{22}, \dot{A}_{22}, \omega_{22}, \dot{\omega}_{22})$ for SXS:BBH:0258 we concluded that these fits are not sufficiently accurate in this corner of the parameter space and that are thus responsible of all outliers.

TABLE VII. SXS outliers with $\bar{\mathcal{F}}^{\max}_{\rm EOB/NR} > 0.2\%$ for TEOBResumSv4.3.0.

#	ID	(q,χ_1,χ_2)	$\bar{\mathcal{F}}^{\max}_{\rm EOB/NR}[\%]$
1	BBH:0258	(1.999666, +0.871258, −0.849486)	0.227161
2	BBH:0292	(2.999266, +0.731359, −0.849301)	0.280737
3	BBH:1453	(2.352106, +0.800164, −0.784292)	0.236153

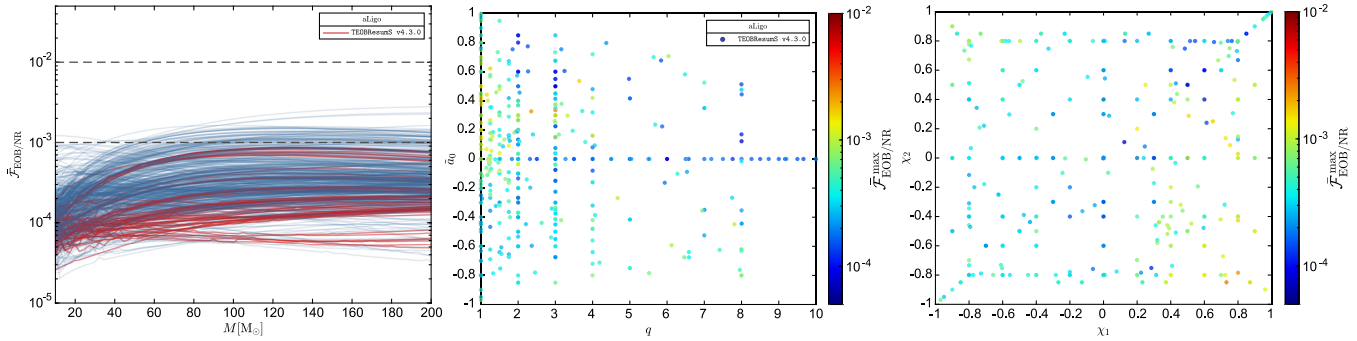

FIG. 17. Performance of TEOBResumSv4.3.0 looking at the EOB/NR unfaithfulness over 534 datasets of the SXS catalog. The model implements a new fit for the unequal-mass part of the function of c_3. Left panel: the EOB/NR unfaithfulness versus the total mass of the binary. Right panel: $\bar{\mathcal{F}}^{\rm max}_{\rm EOB/NR}$ highlighting the dependence on q and $\tilde{a}_0$. Only two configurations are left with $\bar{\mathcal{F}}^{\rm max}_{\rm EOB/NR} > 0.2\%$ that are listed in Table VII.

TABLE VIII. First-guess values for new c_3 values for equal-mass, equal-spin configurations. Together with the unequal-mass configurations of Table VI this gives the TEOBResumSv4.3.1 model whose performance is evaluated in Fig. 18.

#	ID	(q,χ_1,χ_2)	$\tilde{a}_0$	$c_3^{\rm first\ guess}$
1	BBH:1137	$(1,-0.97,-0.97)$	-0.97	89.7
2	BBH:0156	$(1,-0.9498,-0.9498)$	-0.95	88.5
3	BBH:0159	$(1,-0.90,-0.90)$	-0.90	84.5
4	BBH:2086	$(1,-0.80,-0.80)$	-0.80	82
5	BBH:2089	$(1,-0.60,-0.60)$	-0.60	71
6	BBH:2089	$(1,-0.20,-0.20)$	-0.60	52
7	BBH:0150	$(1,+0.20,+0.20)$	$+0.20$	33
8	BBH:0170	$(1,+0.4365,+0.4365)$	$+0.20$	33
9	BBH:2102	$(1,+0.60,+0.60)$	$+0.60$	21.0
10	BBH:2104	$(1,+0.80,+0.80)$	$+0.80$	15.9
11	BBH:0153	$(1,+0.85,+0.85)$	$+0.85$	15.05
12	BBH:0160	$(1,+0.90,+0.90)$	$+0.90$	14.7
13	BBH:0157	$(1,+0.95,+0.95)$	$+0.95$	14.3
14	BBH:0177	$(1,+0.99,+0.99)$	$+0.99$	14.2

Luckily, a way to overcome this problem was already found and discussed in Ref. [36], i.e. computing the quantities useful for the NQC determination directly from the NR-informed model for the postmerger discussed therein. If we do so, the inaccuracies are largely reduced and the resulting waveform is much closer to the one that employs the exact values. In doing so, we realized that the former c_3 fits need a bit of adjustment, which is obtained by simply changing the first-guess value for SXS:BBH:1432 from $c_3^{\rm first-guess} = 25$ to $c_3^{\rm first-guess} = 21$. This eventually yields new fitting coefficients for $c_3^{\neq}$ and a new model, dubbed TEOBResumSv4.3.2, as detailed in the last row of Table IV. The performance of the model versus the SXS catalog is evaluated in Fig. 19. The top row of the figure shows the same analyses as above. We see now that the (minor) changes implemented in the model are such that $\bar{F}^{\rm max}_{\rm EOB/NR} \sim 0.1\%$ all over the catalog. A more careful look at the other plot is in order. Combining the middle and right panel of the first row of Fig. 19, one sees that the model is (relatively)

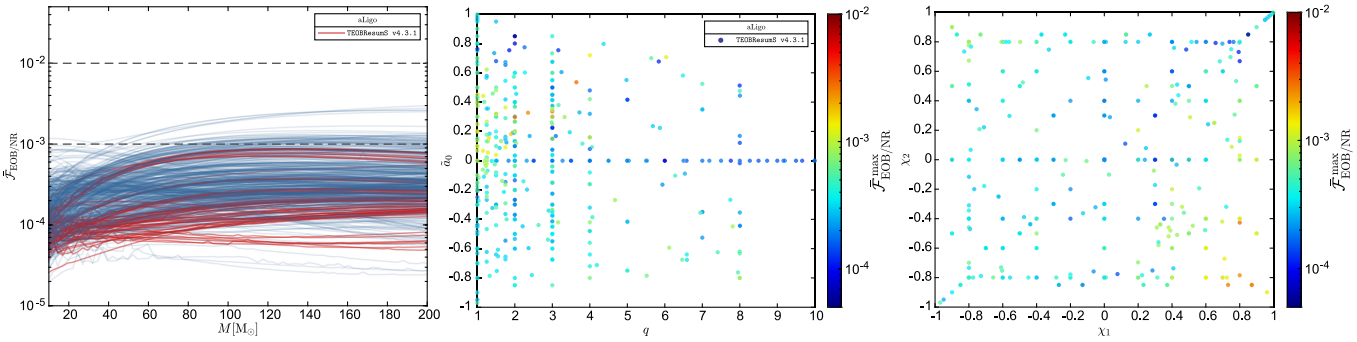

FIG. 18. Performance of TEOBResumSv4.3.1 looking at the EOB/NR unfaithfulness over 534 datasets of the SXS catalog. Despite the global improvement, there are still four outliers above the 0.2% level.

TABLE IX. SXS outliers, with $\bar{\mathcal{F}}^{\max}_{\rm EOB/NR} > 0.2\%$, for TEOBResumSv4.3.1, see Fig. 18. Some configurations are the same as Table V.

No.	ID	(q,χ_1,χ_2)	$\bar{\mathcal{F}}^{\max}_{\rm EOB/NR}[\%]$
1	BBH:2132	(1.999854, +0.871263, −0.849645)	0.258972
2	BBH:0258	(1.999666, +0.871258, −0.849486)	0.257633
3	BBH:1453	(2.352106, +0.800164, −0.784292)	0.247826
4	BBH:0292	(2.999266, +0.731359, −0.849301)	0.273188
5	BBH:1452	(3.641386, +0.800138, −0.426550)	0.294905

less accurate for $1 \leq q \leq 2$ and large spins. Possibly, this is related to the fact that, to determine c_3 we used just ∼10 datasets in that mass ratio range, with spins that are not extremely high. The use of more datasets should be helpful to further reduce $\bar{F}^{\max}_{\rm EOB/NR}$. Modulo this little island, it is worth stressing that the model performs equally well either at *low* and at *large* mass ratios. This is *a priori* expected, also on the basis of the findings of Ref. [52]. It thus does not seem an issue, at least for TEOBResumS, to produce accurate waveforms for large mass ratios. We will come back to discussing this topic below. Let us additionally comment on the bottom row of Fig. 19. To have a better handle on where the improvements are needed most, it is instructive to plot $\bar{\mathcal{F}}^{\max}_{\rm EOB/NR}$ versus $(\hat{S},\hat{S}_*)$ that are the actual spin variables entering the Hamiltonian. The plot indicates that the criticalities mostly occur around the $\hat{S}=\hat{S}_*$ and $\hat{S}_*=0$ lines. This suggests that a new determination of c_3 using NR data along these lines could easily improve the model further. Finally, the middle and rightmost panels in the bottom row of Fig. 19 show the improvement with respect to the original TEOBResumSv4.1.4 model. For convenience, Fig. 20 shows the location in the $(\nu,\tilde{a}_0)$ plane of the 55 SXS simulations used to determine (a^c_6,c_3)

C. Higher modes: Comparisons with NR surrogates

To have a more robust and informative handle on the performance of the new model we conclude this section by comparing it with the NR surrogates NRHybSur3dq8 [51] and NRHybSur2dq15 [84] To do so, we use the *C*, public, implementation of TEOBResumS upgraded with the new a^c_6 fit and c_3 as described above (notably `D3Q3_NQC` of Table II for a^c_6). We compute the waveforms including either only the (2, 2) mode or the (2, 2), (3, 3), (4, 4), and

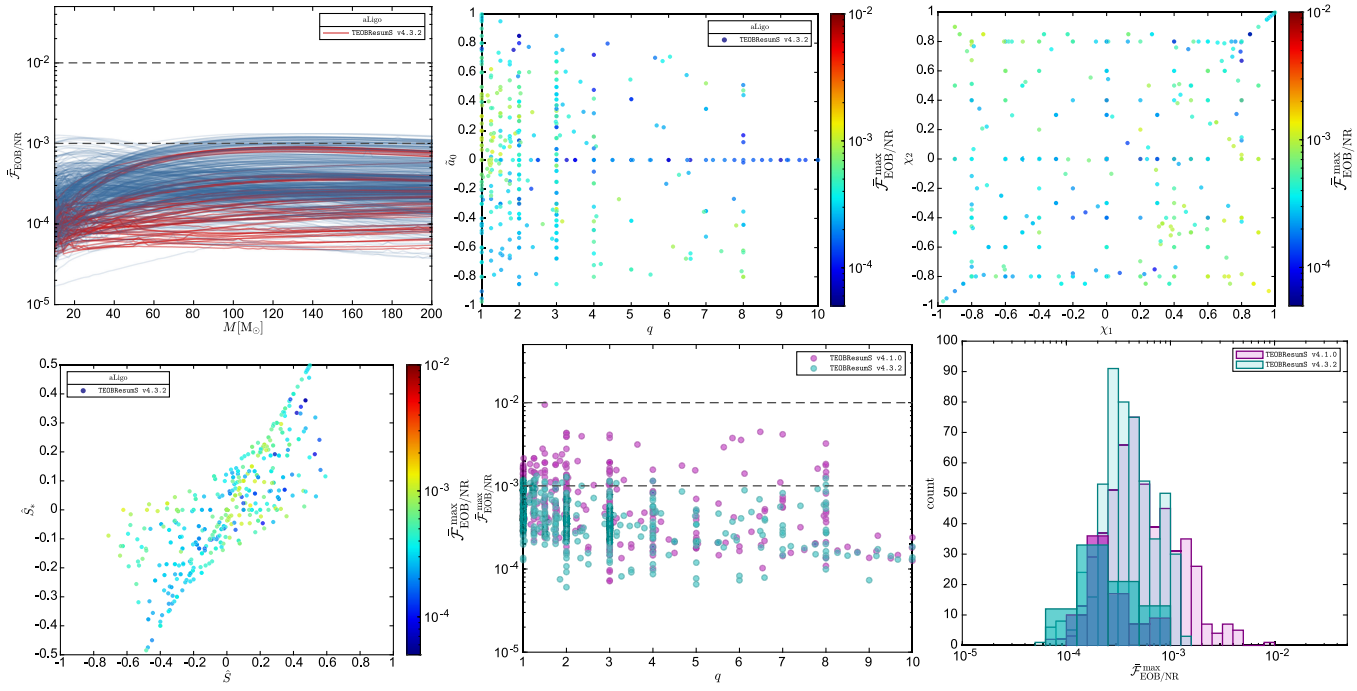

FIG. 19. Final result: the TEOBResumSv4.3.2 model and its performance looking at the EOB/NR unfaithfulness over 534 datasets of the SXS catalog. The differences with respect the original TEOBResumSv4.3.1 model are: (i) the improved analytical representation of a^c_6; (ii) the improved analytical representation of c_3; and (iii) the improved calculation of the NQC corrections based on a more accurate analytical representation of the NR NQC determination point that removes the residual outliers with $0.3 \lesssim \tilde{a}_0 \lesssim 0.6$ found with TEOBResumSv4.3.1. Top left, the EOB/NR unfaithfulness $\bar{\mathcal{F}}_{\rm EOB/NR}$. Top, middle and top right: $\bar{\mathcal{F}}^{\max}_{\rm EOB/NR}$ versus $(\tilde{a}_0,q)$ and (χ_1,χ_2). Bottom, left: $\bar{\mathcal{F}}^{\max}_{\rm EOB/NR}$ versus $(\hat{S},\hat{S}_*)$. Bottom middle and right: comparing $\bar{\mathcal{F}}^{\max}_{\rm EOB/NR}$ of TEOBResumSv4.1.4 and TEOBResumSv4.3.2. The solid histograms refer to nonspinning configurations.

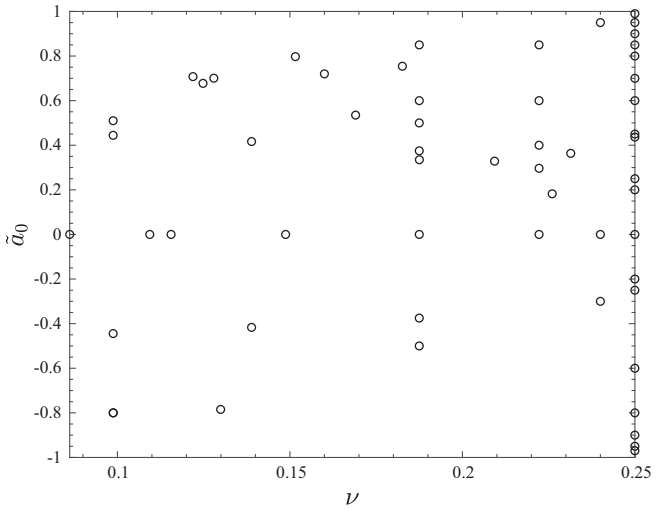

FIG. 20. Location in the $(\nu, \tilde{a}_0)$ space of the 55 SXS simulations used to NR inform the (a_6^c, c_3) functions for TEOBResumSv4.3.2.

(5, 5) subdominant modes.[8] We compute mismatches from 20 Hz and—crucially—to avoid noise in the FFT due to border effects generate the waveforms from 5 Hz, and taper them at the beginning. Notably, while mismatches computed with waveforms constructed from $(\ell, |m|) = (2, 2)$ modes only are independent of the sky position and reference phase of the target waveform (NRHybSur3dq8 or NRHybSur2dq15, in our case), when subdominant modes are included in the waveform construction this simplification does not hold. The usual definition of mismatch depends on the extrinsic parameters of the source. Following, e.g., Refs. [85–88], we define the template sky-maximized (SM) unfaithfulness as

$$\bar{\mathcal{F}}^{\rm SM}_{\rm EOB/NR} = 1 - \max_{t_0^h, \varphi_0^h, \kappa^h} \frac{(s,h)}{\sqrt{(s,s)(h,h)}}, \tag{12}$$

where s is the target waveform, h is our template waveform, κ^h is the template effective polarizability (which encodes information on the sky location of the binary [85,86]) and we fix[9] the target's reference phase $\varphi_0^s = 0$, effective polarizability $\kappa^s = 0$ and inclination $\iota = \pi/3$ between the orbital angular momentum and the line of sight.

[8]It is well known [36] that the (2, 1) and (3, 2) modes are badly modeled for large spins antialigned with the angular momentum due to a nonphysical behavior of the NQC corrections. A way to overcome this problem has been found and is discussed in Ref. [58]. In addition, the (3, 2) mode is not modeled by NRHybSur2dq15, and will therefore not be included in our comparisons.

[9]We have found that the SNR-averaging $\mathcal{F}_{\rm SNR}$ over a grid of κ^s and ϕ^s values typically gives very similar results to the non-averaged unfaithfulness. As such, for computational reasons, we choose to fix κ^s and φ^s.

1. Mass ratio $q \leq 8$

The left panel of Fig. 21 focuses on *nonspinning* systems and displays the (2, 2)-only mismatches computed between TEOBResumSv4.3.2 and NRHybSur3dq8, using the Advanced LIGO noise curve in the frequency interval between [20, 2048] Hz. We consider the NR surrogate in the mass ratio $q \in [1, 8]$, total mass $M \in [40, 150] M_\odot$ and dimensionless spins $|\chi_{1,2}| \leq 0.8$. Mismatches always lie below the 8×10^{-4} threshold, with the largest values of $\bar{\mathcal{F}}^{\rm SM}_{\rm EOB/NR}$ observed for equal mass binaries, for which the effect of radiation reaction is larger causing fewer in-band cycles. When we also explore the spins parameter space (right panel of Fig. 21), we find maximum values of $\bar{\mathcal{F}}^{\rm SM}_{\rm EOBNR}$ around 2×10^{-3}, corresponding to unequal mass systems with large spins. In both cases, more than 99% of the configurations we considered have mismatches below 10^{-3}.

Further considering higher modes (HMs), the scenario remains qualitatively similar, although mismatches degrade overall. Figure 22 summarizes our results, comparing the mismatches obtained with the various binaries and with different mode content. When subdominant modes are included in the construction of the waveform, the median of mismatches distributions shifts to larger values, with ∼75% of the total mismatches below 0.1%. The impact of the (3, 2) and (2, 1) modes is gauged in Fig. 23. As expected, including such modes decreases the overall faithfulness of the model, especially for spinning binaries. As previously discussed, this behavior can be traced back to the unphysical behavior of the NQC for the (2, 1) and (3, 2) modes for systems with large spins antialigned with the orbital angular momentum. This produces an incorrect waveform behavior during the plunge phase up to merger [36]. This result is further investigated in Fig. 24. The plot shows, versus the effective spin $\tilde{a}_0$, the fraction of configurations with $\bar{\mathcal{F}} < \bar{\mathcal{F}}^{\rm thrs}$, where $\bar{\mathcal{F}}^{\rm thrs}$ can take the values indicated in the legend. The (negative) impact of the modes with $\ell \neq m$ is evident, while the performance of the modes with $\ell = m$ is satisfactory.

2. Mass ratio: $8 \leq q \leq 15$

We now repeat the comparison for systems with q up to 15 and $|\chi_1| \leq 0.5$, $\chi_2 = 0$, comparing the NR surrogate NRHybSur2dq15 of Ref. [84] with TEOBResumSv4.3.2, employing the same range of frequencies and total mass used above, as well as the same detector PSD. We consider the NR surrogate in the mass ratio $q \in [8, 15]$, and dimensionless spins $|\chi_{1,2}| \leq 0.5$, $\chi_2 = 0$, corresponding to the validity range of NRHybSur2dq15. The left panel of Fig. 25 shows the (2, 2)-only mismatches for nonspinning systems, while the right panel also explores the impact of spins. Over the set of studied configurations, ∼97% (∼92%) of the mismatches lie below the 10^{-3} threshold for nonspinning (spinning) systems.

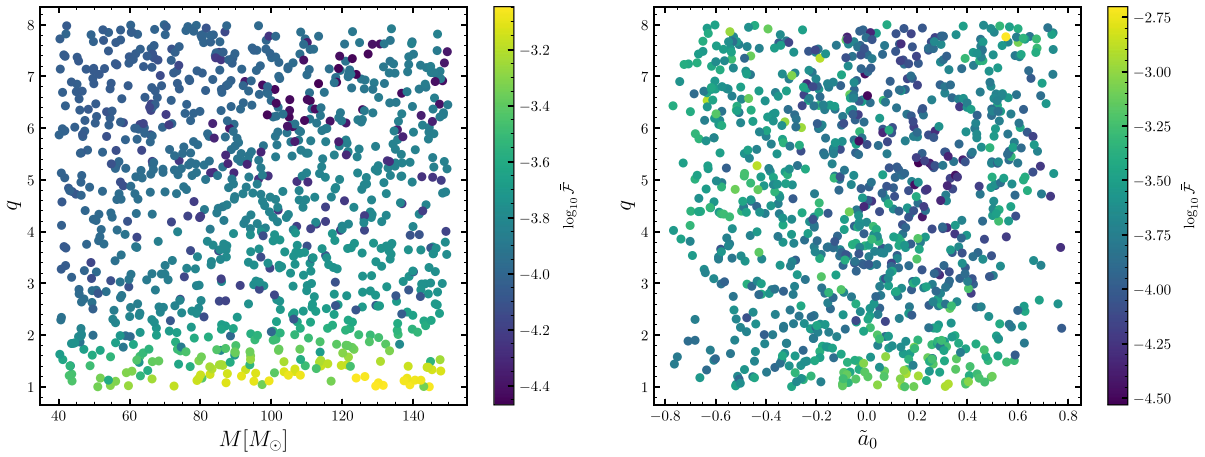

FIG. 21. Left panel: nonspinning configurations. Right panel: aligned spin configurations. Performance of the TEOBResumSv4.3.2 model against the NR surrogate NRHybSur3dq8, including only the $(\ell, |m|) = (2, 2)$ mode. We consider systems with mass ratio $q \in [1, 8]$, total mass $M \in [40, 140] M_\odot$ and dimensionless spins $|\chi_i| < 0.8$ (right panel). The maximal values of $\overline{\mathcal{F}}_{\rm EOB/NR}$ correspond to high mass systems, for which the merger-ringdown gives the largest in-band contribution, and systems with large positive effective spin $\tilde{a}_0$. Notably, however, the largest values of unfaithfulness are at most 2×10^{-3} for both scenarios.

To get a better understanding of the meaning of such values of the mismatches, let us produce a few phasing comparisons with some of the original datasets used to compute the surrogate NRHybSur2dq15. Figure 26 illustrates EOB/NR phasings for $(15, -0.5, 0)$, (15, 0, 0), and $(14, +0.50, 0)$, this latter belonging to the region of the parameter space where the EOB/NR matches with the surrogate have the largest values (top-right panel of Fig. 25).

It is a well-known fact that, when binaries are very asymmetric, the importance of subdominant modes increases. As a consequence, the inclusion of HMs for high mass ratio systems largely impacts the mismatches obtained. Figure 27 compares the mismatches obtained with $(2, |2|)$ modes with those computed using $\ell = m$ modes up to (5, 5) for both spinning and nonspinning configurations. When HMs are employed, mismatches can increase by up to 1 order of magnitude, with 99.4% of them lying below 1% and ∼59% below 0.1%.

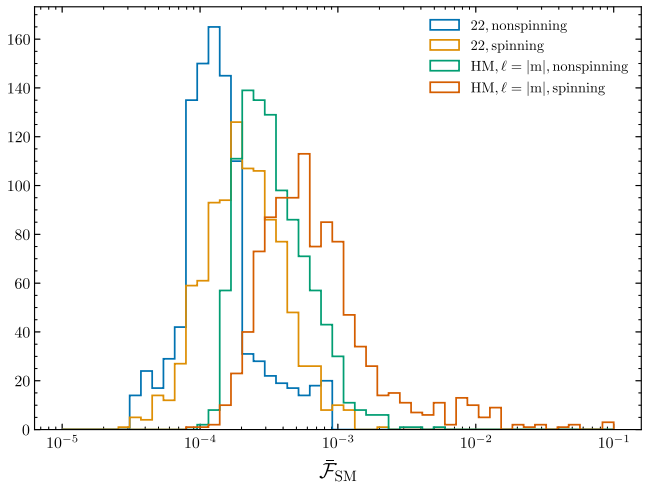

FIG. 22. Summary of all the mismatches computed in this section between TEOBResumS and NRHybSur3dq8. Even when including progressively more information (subdominant modes, spins), the performance of TEOBResumS is overall satisfactory, with ∼97% of mismatches below 1% and 75% below 0.1%.

D. Improving the higher modes: The importance of the $\ell = 2$, $m = 1$ mode

Let us now explore in deeper detail the role of the (2, 1) mode and discuss a way to improve the mode further. As mentioned above and in Ref. [36] (see also Ref. [70]), the problems in the construction of the (2, 1) mode are related to the (incorrect) determination of the NQC corrections. The reason for this is that, by construction, the NQC parameters are determined by imposing continuity between the EOB and NR waveform at some time *after* the peak of each multipole, like the (2, 2) case. However, for the procedure to work, one needs that the NQC functions do not develop any unphysical behavior in the strong-field region close to merger, like poles. In this respect, as already mentioned in Ref. [70], the origin of the unphysical features in the NQC basis for the (2, 1) mode is due to the fact that for antialigned spins the orbital frequency passes through zero and thus, entering at the denominator, introduces a singularity in the functions. Overcoming this difficulty is conceptually simple, as it is sufficient to determine NQC corrections at a moment where the orbital frequency is sufficiently larger than zero so to avoid any pathological behavior. In practice, this means taking as NQC-determination point any time *before* the peak of the (2, 1) mode. The simplest choice (though not the only one) is to do it at the location of the peak of the

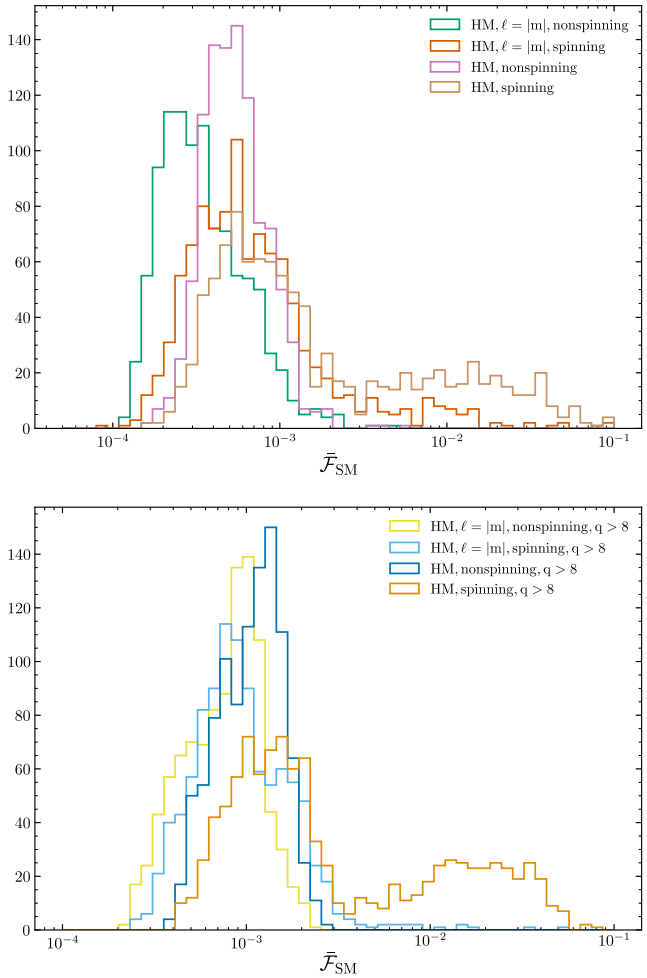

FIG. 23. Comparison between mismatches computed between TEOBResumSv4.3.2 and NRHybSur3dq8 (top) or NRHybSur2dq15 (bottom) with $\ell = |m|$ modes only or with (2, 2), (2, 1), (3, 3), (3, 2), (4, 4), and (5, 5) modes. The inclusion of the (2, 1) and (3, 2) modes shifts the mismatch distribution to higher values, especially when considering spinning binaries. This is due to the performance of the (2, 1) and (3, 2) modes, which are known to display unphysical behavior when spins are large and antialigned with the orbital angular momentum [36].

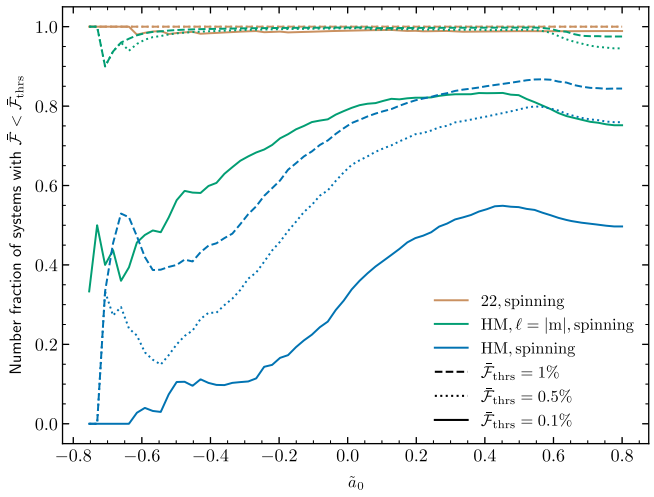

FIG. 24. Summary of the TEOBResumSv4.3.2/NRHybSur3dq8 performance as higher modes are progressively included. Shown is the fraction of configurations with $\bar{\mathcal{F}} < \bar{\mathcal{F}}^{\rm thrs}$, where $\bar{\mathcal{F}}^{\rm thrs}$ can take different values indicated in the legend. The model performs less well as long as the effective spin $\tilde{a}_0$ becomes negative and large. This is mostly due to the (currently inefficient) modelization of modes (2, 1) and (3, 2) during the plunge up to merger in that corner of parameter space.

(2, 2) mode on the EOB time axis, defined as $t^{\rm EOB}_{A^{\rm max}_{22}}$. In practice, this needs to extend the ringdown model also before the peak of (2, 1), which implies that the NR-informed fits discussed in Ref. [36] are not useful for this purpose and should be redone. However, the approach of NR informing the ringdown from $t^{\rm EOB}_{A^{\rm max}_{22}}$ for *all* modes was followed in all SEOBNR waveform models that incorporated higher modes [35,67]. In particular, Ref. [35] gives updated NR-informed fits that describe the ringdown for several waveform modes (up to $\ell = 5$) starting from $t^{\rm NR}_{A^{\rm max}_{22}}$ instead of $t^{\rm NR}_{A^{\rm max}_{\ell m}}$ as it is normally done for TEOBResumS.

Let us briefly review the general procedure for modeling the ringdown that is adopted by TEOBResumS and SEOBNR, which relies on the procedure of Ref. [89]. The difference in the two model families is discussed below. For each waveform mode, one fits the quasi-normal-modes (QNM)-rescaled waveform

$$\bar{h}_{\ell m} = h^{\rm rng}_{\ell m} e^{+\sigma_{\ell m}\tau}, \tag{13}$$

where $h^{\rm rng}_{\ell m}$ is the numerical ringdown waveform, $\sigma = \alpha_1 + i\omega_1$ is the fundamental complex QNM frequency and $\tau = t - t^{\rm match}_{\ell m}$. The QNM-rescaled wave is then written as $\bar{h} = A_{\bar{h}} e^{i\phi_{\bar{h}}}$, where h is always ν normalized and

$$A_{\bar{h}} = c^A_1 \tanh\left(c^A_2 \tau + c^A_3\right) + c^A_4, \tag{14}$$

$$\phi_{\bar{h}} = \phi_0 - c^\phi_1 \log\left(\frac{1 + c^\phi_3 e^{-c^\phi_2 \tau} + c^\phi_4 e^{-2c^\phi_2 \tau}}{1 + c^\phi_3 + c^\phi_4}\right), \tag{15}$$

where we adopt the notation[10] introduced in Ref. [89]. In passing, we also remind the reader that the fitting provided

[10]Note that in the SEOBNR family, notably in Refs. [35,66], uses precisely the same functional form introduced in Ref. [89] but the coefficients are named differently (and one omitted). More precisely, for the amplitude, one has $\{c^A_1 = c^{\ell m}_{1,c}, c^A_2 = c^{\ell m}_{1,f}, c^A_3 = c^{\ell m}_{2,f}, c^A_4 = c^{\ell m}_{2,c}\}$, while for the phase $\{c^\phi_1 = d^{\ell m}_{1,c}, c^\phi_2 = d^{\ell m}_{1,f}, c^\phi_3 = d^{\ell m}_{2,f}, c^\phi_4 = 0\}$. Moreover, consider that there are some different sign conventions; for the QNM frequencies we have $\alpha_1 = -\sigma^R_{\ell m}$ and $\omega_1 = -\sigma^I_{\ell m}$, and in our case the waveform frequency is defined as positive, while the one used in Eq. (53) of Ref. [35] is negative. Although we adopt the fits of Ref. [35] we prefer to stick to the notation of Ref. [89] for consistency with previous work.

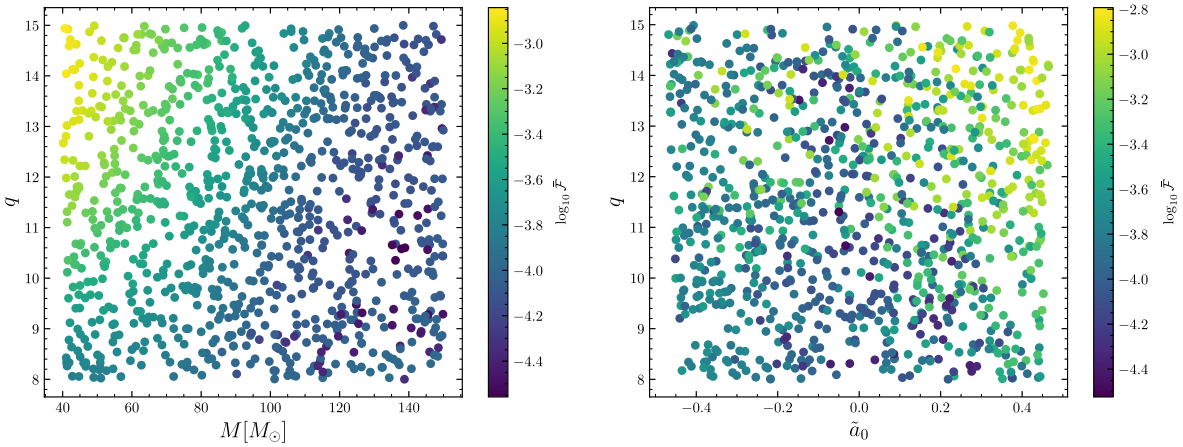

FIG. 25. Performance of TEOBResumSv4.3.2 against the NRHybSur2dq15 NR surrogate, including only the $(\ell, |m|) = (2, 2)$ mode. We consider systems with mass ratio $q \in [8, 15]$, total mass $M \in [40, 140] M_\odot$, zero spins (left panel) or aligned spins with dimensionless spin magnitudes $|\chi_1| < 0.5$ and $\chi_2 = 0$ (right panel). The largest values of unfaithfulness ($\bar{\mathcal{F}} \sim 10^{-3}$) are found for unequal mass systems with large, positive, spin.

by Eq. (14) is not suitable for large mass ratios, as discussed in Refs. [58,90]. To ensure continuity, some coefficients are constrained and are linked to NR quantities. Here, the two EOB families adopt different strategies. In particular, TEOBResumS adopts the strategy outlined in Refs. [36,89], imposing the constraints at the peak of the (ℓ, m) amplitude for each mode and constraining $(c_1^A, c_2^A, c_4^A, c_1^\phi, c_2^\phi)$ in terms of QNM frequencies, $A_{\ell m}^{\max}$ and $\omega_{\ell m}^{\max}$. On the other hand, the SEOBNR family imposes continuity conditions always at the peak of the quadrupolar amplitude for each mode; this results in the constraints [35,67]

$$c_1^A = (\dot{A}_{t_{\ell m}^{\rm match}} + \alpha_1 A_{t_{\ell m}^{\rm match}}) \cosh^2 c_3^A / c_2^A, \tag{16}$$

$$c_4^A = A_{t_{\ell m}^{\rm match}} - (\dot{A}_{t_{\ell m}^{\rm match}} + \alpha_1 A_{t_{\ell m}^{\rm match}}) \cosh c_3^A \sinh c_3^A / c_2^A \tag{17}$$

$$c_1^\phi = (\omega_1 - \omega_{t_{\ell m}^{\rm match}}) \frac{1 + c_3^\phi}{c_2^\phi c_3^\phi}, \tag{18}$$

$$c_4^\phi = 0, \tag{19}$$

which leave as free coefficients $(c_2^A, c_3^A, c_2^\phi, c_3^\phi)$.

In the following, we proceed implementing the SEOBNR strategy for some of the higher modes. We obtain the fitted coefficients $(c_2^A, c_3^A, c_2^\phi, c_3^\phi)$ and the NR quantities $(A_{t_{\ell m}^{\rm match}}, \dot{A}_{t_{\ell m}^{\rm match}}, \omega_{t_{\ell m}^{\rm match}})$ from the global fits presented in Ref. [35] (see Appendixes C and D therein). Although our main goal here is to fix the behavior of the EOB (2, 1) mode, we will also consider modes (3, 3) and (4, 4) to gain more precise insights on the relevance of tiny details in ringdown modeling.

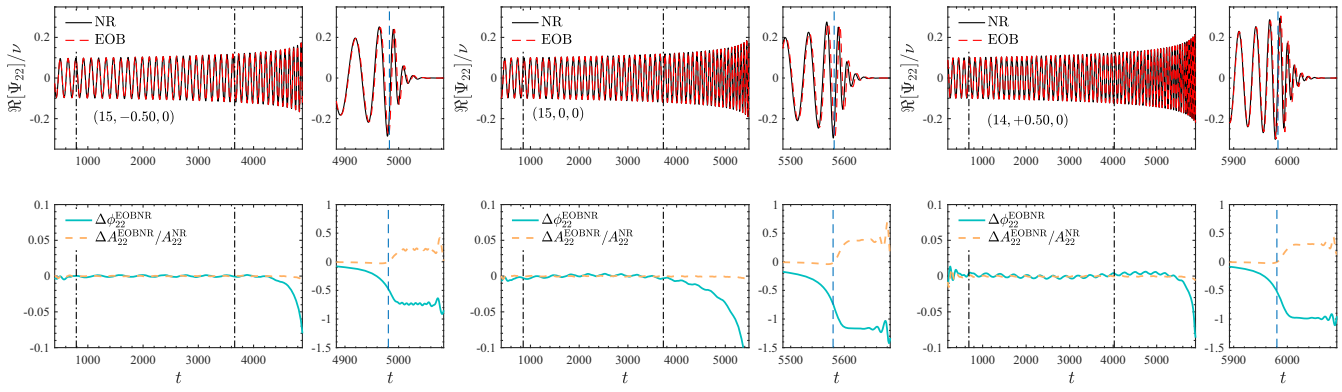

FIG. 26. EOB/NR phasing comparisons with some of the SXS simulations of Ref. [84] used to construct the NRHybSur2dq15 NR surrogate. Note that the accumulated phase difference is substantially independent of the spin value. The origin of the EOB/NR discrepancies might be due to missing physics in the analytical description of the fluxes, as advocated in Ref. [52]. Despite the phase differences may look large, $\bar{\mathcal{F}}^{\max}_{\rm EOB/NR} \sim 10^{-3}$ for these configurations, see Fig. 25.

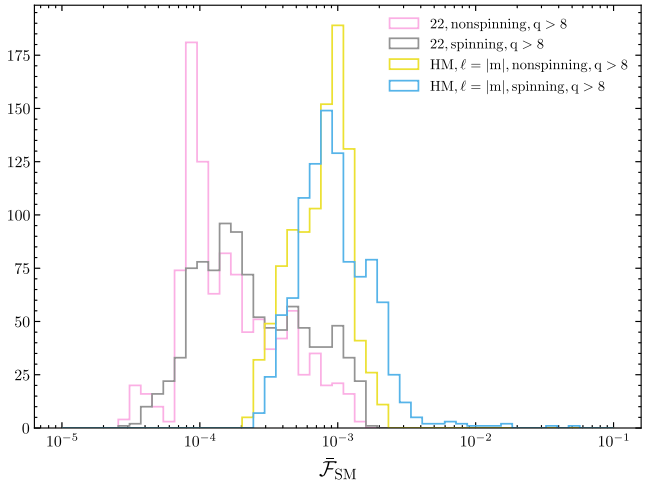

FIG. 27. Summary of all the mismatches computed in this section between TEOBResumSv4.3.2 and NRHybSur2dq15. When considering spinning systems including subdominant modes with $\ell = |m|$, we find ∼99.3% of mismatches below 1%.

Figure 28 highlights the improvement in the total EOB/NR unfaithfulness brought by replacing *only* the (2, 1) ringdown part with the one of Ref. [35]. The other modification implemented is that NQC corrections are now determined at $t^{\rm EOB}_{A^{\rm max}_{22}}$, though using the same NQC basis that was used before. One appreciates how the number of configurations with $\bar{\mathcal{F}}_{\rm SM} < 0.01$ (solid lines) is now much smaller than before (dashed lines). A better insight in the accuracy of the model is given by Figs. 29 and 30. The first figure shows that the correct modelization of the (2, 1) mode is essential. By contrast, the impact of changes in the (3, 3) and (4, 4) modelization is marginal and in fact found to slightly worsen the global performance of the model (see the violet violin plots in Fig. 29). Figure 30 reports the values of the unfaithfulness maximized and minimized as the total mass M is varied between $40M_\odot$ and $200M_\odot$. The largest values of unfaithfulness are typically obtained for heavy binaries ($M > 100M_\odot$), indicating that the modelization of the transition from late plunge to merger ringdown needs further improvements. More precisely, Fig. 31 offers an insight on the distribution of the total-mass-averaged mismatches in the two-dimensional parameter space of q and $\tilde{a}_0$. We find that the largest mismatches are obtained for systems with large mass ratio $q > 4$ and large spins $|\tilde{a}_0| > 0.5$. In these cases, the degradation of the performance of the model can be attributed to the modelization of the (3, 3) and (4, 4) modes close to merger. Overall, ∼98% (99%) of the total-mass-maximized mismatches lie below the 3% threshold when $q < 8$ ($q > 8$).

1. Interference between corotating and counterrotating QNMs for (2, 1) and (3, 2) modes

Now that we have seen the changes brought by the improvement of the (2, 1) mode, we turn our attention to

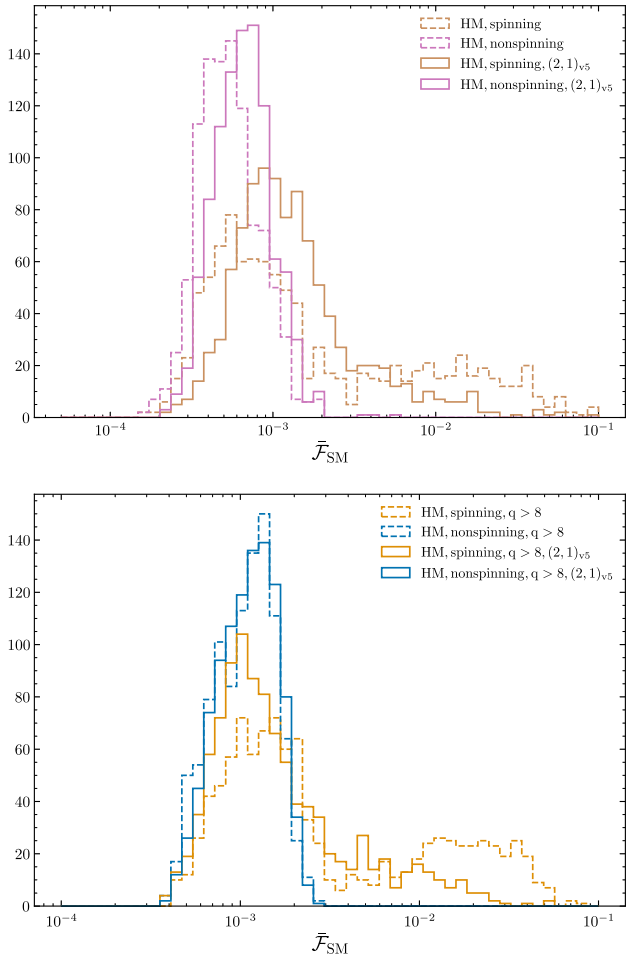

FIG. 28. Relevance of the (2, 1) mode. Unfaithfulness comparison between TEOBResumSv4.3.2 and NRHybSur3dq8 (top panel) or NRHybSur2dq15 (bottom panel) with the (2, 2), (2, 1), (3, 3), (3, 2), (4, 4), and (5, 5) modes, using either the previous prescription for the NQCs and merger/ringdown of the (2, 1) mode or the one from SEOBNRv5 [35]. The high mismatch tail of the distribution almost disappears when employing this latter.

other physical elements that may affect the accuracy of the higher modes in our model. In particular, we will focus on mode mixing. There are two kinds of mode mixing that occur when considering the ringdown of rotating black holes. The first one is due to the contribution of the counterrotating QNMs, i.e. to the modes with $m < 0$. The late behavior of this effect can be modeled considering only the fundamental corotating and counterrotating QNMs, as detailed in Refs. [58,73,91,92]. The second kind of mixing occurs between modes with the same m but different ℓ, as noted in Ref. [93]. This occurs because the waveform modes are written using the spherical harmonic basis ${}_{-2}Y_{\ell m}$, while the natural base for the QNMs is the spheroidal harmonic one, ${}_{-2}S_{\ell mn}$. We model this mode mixing for the (3, 2) and (4, 3) modes as done in SEOBNR_v5, following the approach outlined in Sec. III C of Ref. [35], whose main ideas are recalled here (see also Ref. [94]). Reliable relations between

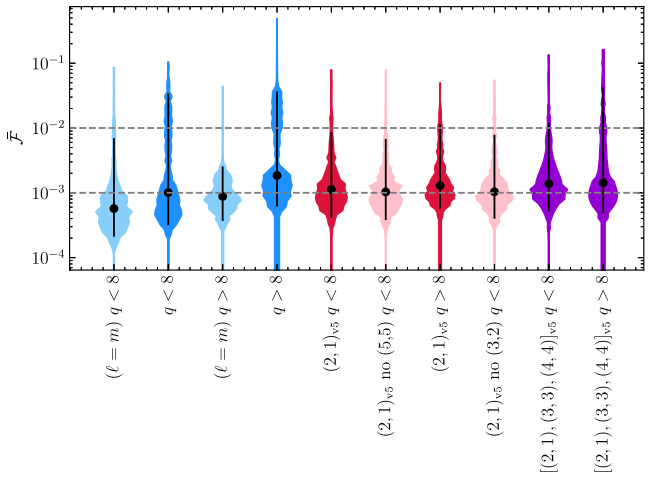

FIG. 29. Comparison between mismatches computed between TEOBResumSv4.3.2 and NRHybSur3dq8 ($q < 8$) or NRHybSur2dq15 ($q > 8$) with different mode content and various strategies for the computation of the (2, 1), (3, 3), and (4, 4) modes.

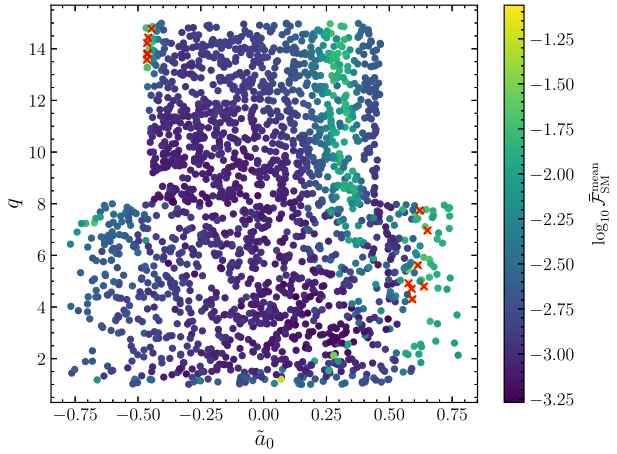

FIG. 31. Mass-averaged mismatches computed between TEOBResumSv4.3.2 and NRHybSur3dq8 ($q < 8$) or NRHybSur2dq15 ($q > 8$) for configurations with varying mass ratio and spins. Red crosses indicate systems for which the average unfaithfulness lies above the 3% threshold. Such cases are typically characterized by large values of q and large $|\tilde{a}_0|$.

spheroidal ${}^{S}h_{\ell m}$ and spherical $h_{\ell m}$ modes can be obtained neglecting the contributions of the overtones and considering only contribution of the $\ell' < \ell$ modes. Once the relations are found, the numerical spheroidal modes are extracted from the spherical ones and fitted using the usual templates of Eqs. (14) and (15). The coefficients found with the primary fits of the spheroidal modes are then fitted over the parameter space, so that the spheroidal ringdown can be reconstructed from the global fits. Then to obtain the spherical modes it is sufficient to invert the spheroidal-spherical relations.

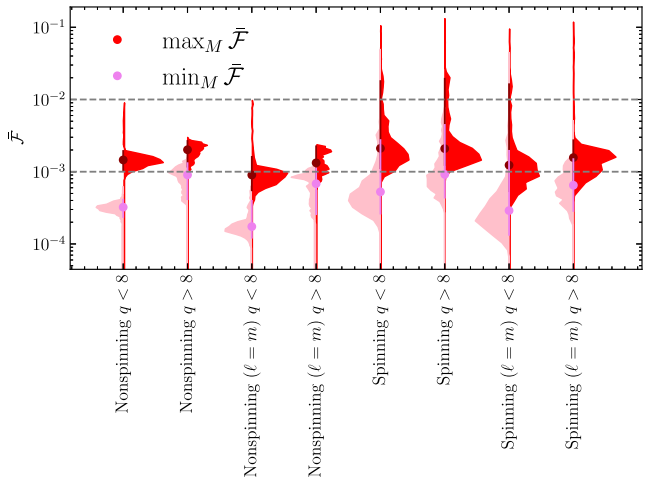

FIG. 30. Total mass maximized (red) or minimized (pink) mismatches computed between TEOBResumSv4.3.2 and NRHybSur3dq8 ($q < 8$) or NRHybSur2dq15 ($q > 8$). We consider here the same 1000 configurations of mass ratio (and spins) employed within the rest of the paper, and vary the total mass between 40 and 200 solar masses.

The inclusion of these effects in the complete EOB model requires several modifications and testing of the TEOBResumS infrastructure that we postpone to future work. Here we just test the NR-informed ringdown waveform of Ref. [35] in a significative case. We consider the NR simulation BBH:1375 of the SXS catalog [95], which corresponds to a BBH with $(q, \chi_1, \chi_2) = (8, -0.9, 0)$. Figure 32 shows the waveform and the frequency (black) for the (2, 1) and (3, 2) modes of the aforementioned

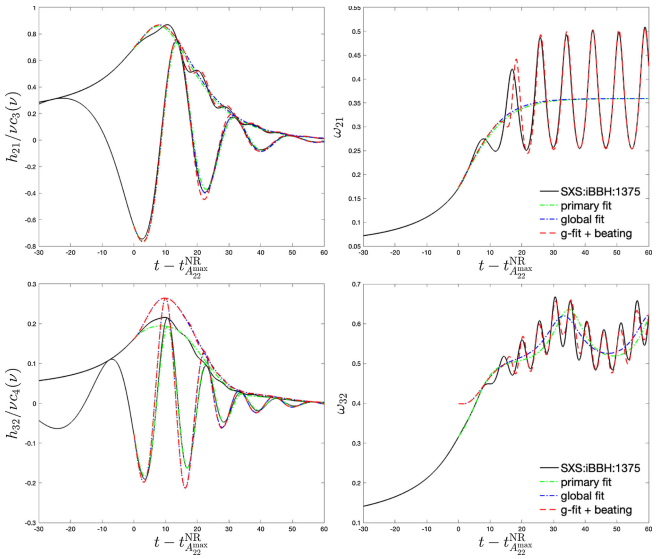

FIG. 32. Configuration $(8, -0.9, 0)$, beating (mode mixing) between different QNMs. Top panel: mode (2, 1) with and without the interference between corotating and counterrotating QNMs. Bottom panel: same effect for the (3, 2) mode superposed to the modulation due to the mixing between (2, 2) and (3, 2) QNMs.

configuration, compared with different analytical prescriptions. Note that in this figure the multipoles are normalized with $c_{\ell+\epsilon} = X_2^{\ell+\epsilon-1} + (-)^m X_1^{\ell+\epsilon-1}$, where ϵ is the parity of the mode (0 if $\ell + m$ is even, 1 otherwise). From the analytical point of view, we consider different prescriptions. We start by showing in green the waveform obtained with the primary fits; for the (2, 1) multipole it is simply obtained fitting the numerical spherical mode, while for the (3, 2) spherical mode it is obtained combining the fit of the spheroidal (3, 2) mode and of the spherical (2, 2) mode, as discussed above. We also show in blue the waveform obtained with the global fits of Ref. [35] (see Appendixes C and D therein). While for the (2, 1) mode this waveform is comparable to the one obtained directly with the primary fit, the (3, 2) waveform obtained from the global fits is less accurate for what concerns the amplitude. This seems to suggest that in this specific region of the parameter space the global fits of Ref. [35] do not provide precise values and might need some improvements. However, despite this inaccuracy the waveform is still qualitatively reliable, and in particular is able to catch the frequency modulation due to the $m = 2$ mode mixing. Finally, we also show in red the waveform in which we have included the beating between corotating and counterrotating fundamental QNMs; the coefficients needed to reproduce this effect are extracted from the numerical waveform (see Ref. [58] for more details). In this case, we are also able to reproduce the higher-frequency oscillations in the multipole frequency, both in the (2, 1) and (3, 2) multipoles. Such proof of principle study thus indicates that, provided a number of NR waveforms well placed in the parameter space, all mode-mixing effects can be modeled at a reasonable level of accuracy.

VI. CONCLUSIONS

The basic guiding principle behind the construction of robust and flexible EOB models is to explore, one by one, each physical element entering the construction of the model [73]. At the dawn of the development of EOB models this guiding principle was followed carefully because of the need for understanding in detail the effect of each analytical choice and its impact on describing accurately the physics of the plunge and merger. However, in the rush of constructing waveform models with higher and higher NR faithfulness, the original attitudes have progressively lost importance. In particular, the attitude of using automatized calibration procedures involving several parameters at the same time [35,66,67] may eventually hide the importance of each analytical element of the model. Although some recent studies in this direction were attempted recently (see, e.g. [34,60,96]) the role of some building blocks of the procedure of NR-informing EOB models (and in particular TEOBResumS) was not spelled out systematically so far. The understanding of the impact of each building block within the EOB construction can be rephrased as *understanding waveform analytic systematics*. To make well-precise statements around the concept of waveform systematics within the EOB formalism, we focused on some pivotal building blocks of the models and illustrated how a careful mastery of their properties is important to yield improved waveform accuracy. We mainly considered *nonspinning* binaries and analyzed the importance of either the NR tuning of the EOB flexibility parameters or the impact of high-order PN terms in the EOB (radial) potentials. Our findings can be summarized as follows:

(i) We have shown that a more precise way of NR informing the effective 5PN function $a_6^c(\nu)$ allows us to improve the performance of TEOBResumS (on nonspinning SXS data) of at least a factor 2 with respect to current state of the art: the maximum value of the EOB/NR unfaithfulness (on the Advanced LIGO PSD) is lowered to $\sim 5 \times 10^{-4}$. We remark that this is obtained by NR tuning the *single* function $a_6^c(\nu)$.

(ii) In order to better understand the potentialities of the model, we have also attempted to NR tune the time interval $\Delta t_{\rm NQC}$ that, loosely speaking, defines the merger location on the EOB time axis. This procedure is similar to the one routinely adopted in SEOBNR models [66], although the precise understanding of the impact of each element was not spelled out so far. For the illustrative $q = 1$ case, we found that the tuning of $\Delta t_{\rm NQC}$ allows one to reduce the EOB/NR phase difference of about a factor 2 during plunge and merger (see Fig. 4). Unfortunately, this also yields a slight, though noticeable, degradation of the phasing performance of the model during the inspiral. For this reason, we generally advocate to *avoid* using $\Delta t_{\rm NQC}$ as an NR-informed parameter. In addition, the advantages in terms of EOB/NR unfaithfulness look so small with respect to tuning only a_6^c that it does not seem worth introducing such complication in the TEOBResumS model. We stress, however, that in principle one *should* tune $\Delta t_{\rm NQC}$ in a way that it is compatible with the test-mass case (see e.g. [55]). Given the subtlety of this approach, we defer it to forthcoming studies.

(iii) We then explored whether the use of recently obtained (quasicomplete) 5PN information in the D and Q EOB potentials helps to obtain a model as flexible and as accurate as the standard one (with or without iteration on next-to-quasicircular waveform amplitude corrections). We highlighted that the performance of a (nonspinning) EOB waveform model crucially depends on the NR-faithful modelization of noncircular effects during the plunge up to merger. The new, and *a priori* unexpected, finding is that NR-informed NQC corrections, which are

purely phenomenological, are practically equivalent to analytically known noncircular effects entering the noncircular sector of the Hamiltonian. The fact that the NR-informed NQC iterations are crucial aspects of the model suggests that, possibly, genuine noncircular effects in the waveform (e.g. the leading-order ones as implemented in the eccentric model [97]) could be useful to improve the EOB/NR agreement further during the late plunge up to merger.

(iv) Thanks to our enhanced understanding of noncircular effects in the strong field (and in particular of the radial force $\mathcal{F}_r$), we present a slightly modified version of the eccentric model of Ref. [34], although for the moment only limited to nonspinning binaries. This model presents slightly improved matches with the SXS eccentric simulations available as well as an excellent EOB/NR agreement for the scattering angle for strong-field configurations. The extension to spins is postponed to future work as it requires an improvement of the description of spin-orbit interaction for large, positive, spins, as already pointed out in Ref. [34].

(v) We then obtained several new versions of the TEOBResumS model for spin-aligned binaries that rely on the newly determined a_6^c and (essentially) only differ by the NR-informed effective N^{3}LO function c_3. Eventually, by changing only a_6^c and c_3 with respect to the TEOBResumS default choices [14,36], we obtain a highly NR-faithful new model, dubbed TEOBResumSv4.3.2, which has maximal EOB/NR unfaithfulness $\mathcal{F}^{\max}_{\rm EOB/NR} \sim 10^{-3}$ for the (2, 2) mode all over the publicly available SXS catalog. This seems to suggest that TEOBResumSv4.3.2 is currently the EOB waveform model with the lowest EOB/NR unfaithfulness, compatible with the SEOBNRv5 model [35]. It must be noted, however, that some of the NR datasets of Ref. [35] for large mass ratios are not public, so that we could not perform an actual apple-with-apple comparison. To comply with the spirit of this paper, we also kept all incremental steps that brought us to obtain TEOBResumSv4.3.2, i.e. we kept track of four different EOB models, summarized in Table IV, which always have $\mathcal{F}^{\max}_{\rm EOB/NR} \lesssim 4 \times 10^{-3}$ and differ from details in the representation of the c_3 function. Each one of these models can be used in injection/recovery studies to explore how such small differences in EOB/NR mismatches impact the unbiased recovery of injected parameters. We finally want to remark that the values of the NR-informed parameters were obtained using simple procedures. For example, the first-guess c_3 values, were obtained only by visual inspection of the time-domain phasings and then similarly fitted using simple fitting functions. Notably, the number of NR datasets used to do so is only composed by eight nonspinning and 47 spin-aligned datasets, for a total of 55. This amounts to only the 10.3% of the public SXS waveform catalog. We also note that the calculation of mismatches only occurs as a validation check *a posteriori* of the model. We remark that this is different from other approaches [66] where the NR calibration is done on the EOB/NR mismatches themselves. This seems to indicate that the analytical structure of TEOBResumS (in all its avatars) is robust and a relatively moderate amount of NR information is needed to determine the dynamical parameters.[11]

(vi) We also validated the TEOBResumSv4.3.2 model against two NR surrogate models, NRHybSur3dq8 and NRHybSur2dq15, i.e. up to mass ratios $q = 15$. When focusing on the $(\ell, |m|) = (2, 2)$ mode, our results reflect the previous investigations performed against NR directly. The mismatches with NRHybSur2dq15 are at most $\sim 10^{-3}$, despite no NR simulations were used to inform the model for $q \geq 10$. This finding is also consistent with previous NR validation of TEOBResumS, in the nonspinning case only, for intermediate-mass-ratio binaries [52], notably up to $q = 100$. When higher modes are additionally included, the performance of the model degrades for systems with high mass ratio and large spin magnitudes. Appropriate modeling of the (2, 1) and (3, 2) modes, especially, appears critical (notably, for antialigned spins) in order to obtain mismatches below 10^{-2}. This is in line with previous findings using TEOBResumS [36]. The accurate modelization of (2, 1), (3, 2), as well as (4, 3), modes during the plunge up to merger is known to be the current Achilles' heel of the model. This is fundamentally related to the current implementation of NQC waveform corrections that do not work for those configurations where the orbital frequency Ω crosses zero. This is a standard feature that occurs for certain configurations with antialigned spins and that is present also in the test-mass limit [69]. Note, however, that in SEOBNR models [35,67] this problem is efficiently avoided because the ringdown of each (ℓ, m) mode is matched at the peak of the (2, 2) mode and not at the peak of the (ℓ, m) waveform mode itself. As a pragmatical solution to this long-standing issue, we implemented within TEOBResumS the (2, 1) mode of the SEOBNRv5 model, precisely in the form described in Ref. [35]. This by itself is sufficient, as shown in Fig. 28, to have more than the 98% of the total-mass-maximized unfaithfulness to lie below the 3% threshold when comparing to the surrogate models. In this respect, we also remind the reader that of the important features of the NR (2, 1)

[11]Note that a separate issue is the modeling of postpeak (ringdown) waveform. Here we rely on the model of Ref. [36], which was obtained using a large number of simulations for convenience, despite the evident redundancy of many datasets.

waveform amplitude, i.e. which can develop a zero during the late inspiral for certain special configurations of the spins [67], is naturally accounted for by the TEOBResumS, resummed, waveform (see [36], Fig. 15), without the need for resorting to NR calibration (note that this seems partly necessary for the SEOBNR models [35,67]). Moreover, in the spirit of understanding the impact of the ringdown modelization on the global performance of the model, in Figs. 29 and 30 we explore the relevance of using different representations for the ringdown of the (4, 4) and (3, 3) modes. We also preliminarily investigate the impact of mode mixing in the ringdown of TEOBResumS, adopting the modelization of Ref. [35] and improving it further by additionally incorporating corotating and counterrotating QNMs (see Fig. 32) in the spirit of Ref. [58]. The complete modelization of QNMs mode mixing in the (3, 2), and possibly also (4, 3), modes all over the parameter space is however postponed to future work.

(vii) Finally, our detailed analysis of the nonspinning case in Fig. 1 indicates that, assuming that NR is *exact*, TEOBResumSv4.3.2 has to gain *only* between 0.1 and 0.2 rad at merger to obtain EOB/NR unfaithfulnesses *below* 10^{-4} for present (and future) ground-based detectors. In particular, we remark that our simple study highlights that this phasing loss only occurs in the last orbit before merger. Although some studies claim that the accuracy of NR simulations should be improved further by at least 1 order of magnitude in terms of unfaithfulness [2], improving the EOB phasing by 0.2 rad around merger looks like an easy task as it seems to be mostly controlled by the NR-informed functions than by high-order contributions to the EOB potentials. In this respect, we recall that the NR-informed NQC corrections, which are key to correctly shape the EOB waveform at merger, are currently not very sophisticated, as one only imposes the EOB/NR consistency between $(\omega_{22}, \dot{\omega}_{22}, A_{22}, \dot{A}_{22})$, but there are *no* conditions imposed on second-order time derivatives. Preliminary investigations in the test-mass limit [58] suggest that additional noncircular corrections (either NR informed or built in due to the use of the native generic Newtonian prefactor in the waveform) may play an important role in improving the analytic waveform behavior up to merger. This is discussed extensively in Ref. [58].

The improvements introduced in TEOBResumS-GIOTTO in this work are automatically available to calculate spin precessing BBH waveforms [10,15], binary neutron star waveforms [23,98,99], and black-hole–neutron-star waveforms [25].

TEOBResumS is developed open source and publicly available [100]. The code uses semantic versioning and the versions (`v?.?.?`) used in this work correspond to the code tags on the master branch. TEOBResumS can also be installed via `pip install teobresums`. The code is interfaced to state-of-art gravitational-wave data-analysis pipelines: BAJES [101], Bilby [102] and PyCBC [103].

ACKNOWLEDGMENTS

We are grateful to J. Yoo, V. Varma, M. Giesler, M. Scheel, C. J. Haster, H. P. Pfeiffer, L. Kidder, and M. Boyle for sharing with us the SXS simulations presented in Ref. [84]. P. R. is supported by the Italian Minister of University and Research (MUR) via the PRIN 2020KB33TP, Multimessenger astronomy in the Einstein Telescope Era (METE). P. R. and A. A. acknowledge the hospitality of the Institut des Hautes Etudes Scientifiques where part of this work was done. R. G. is supported by the Deutsche Forschungsgemeinschaft (DFG) under Grant No. 406116891 within the Research Training Group RTG 2522/1. A. A. has been supported by the fellowship Lumina Quaeruntur No. LQ100032102 of the Czech Academy of Sciences. S. B. acknowledges support by the EU H2020 under ERC Starting Grant No. BinGraSp-714626 and by the EU Horizon under ERC Consolidator Grant No. InspiReM-101043372. The present research was also partly supported by the "2021 Balzan Prize for Gravitation: Physical and Astrophysical Aspects," awarded to Thibault Damour. We are also grateful to P. Micca for inspiring suggestions. Calculations were performed on the Tullio server at INFN, Torino.

[1] T. B. Littenberg, J. G. Baker, A. Buonanno, and B. J. Kelly, Phys. Rev. D **87**, 104003 (2013).
[2] M. Pürrer and C.-J. Haster, Phys. Rev. Res. **2**, 023151 (2020).
[3] R. Gamba, M. Breschi, S. Bernuzzi, M. Agathos, and A. Nagar, Phys. Rev. D **103**, 124015 (2021).
[4] C. B. Owen, C.-J. Haster, S. Perkins, N. J. Cornish, and N. Yunes, Phys. Rev. D **108**, 044018 (2023).
[5] J. S. Read, Classical Quantum Gravity **40**, 135002 (2023).
[6] A. Buonanno and T. Damour, Phys. Rev. D **62**, 064015 (2000).

[7] T. Damour, P. Jaranowski, and G. Schaefer, Phys. Rev. D **62**, 084011 (2000).
[8] T. Damour, Phys. Rev. D **64**, 124013 (2001).
[9] T. Damour, P. Jaranowski, and G. Schäfer, Phys. Rev. D **91**, 084024 (2015).
[10] S. Akcay, R. Gamba, and S. Bernuzzi, Phys. Rev. D **103**, 024014 (2021).
[11] S. Schmidt, M. Breschi, R. Gamba, G. Pagano, P. Rettegno, G. Riemenschneider, S. Bernuzzi, A. Nagar, and W. Del Pozzo, Phys. Rev. D **103**, 043020 (2021).
[12] A. Nagar, P. Rettegno, R. Gamba, and S. Bernuzzi, Phys. Rev. D **103**, 064013 (2021).
[13] S. Ossokine *et al.*, Phys. Rev. D **102**, 044055 (2020).
[14] G. Riemenschneider, P. Rettegno, M. Breschi, A. Albertini, R. Gamba, S. Bernuzzi, and A. Nagar, Phys. Rev. D **104**, 104045 (2021).
[15] R. Gamba, S. Akçay, S. Bernuzzi, and J. Williams, Phys. Rev. D **106**, 024020 (2022).
[16] R. Gamba, S. Bernuzzi, and A. Nagar, Phys. Rev. D **104**, 084058 (2021).
[17] R. Gamba, M. Breschi, G. Carullo, P. Rettegno, S. Albanesi, S. Bernuzzi, and A. Nagar, Nat. Astron. **7**, 11 (2023).
[18] A. Ramos-Buades, A. Buonanno, M. Khalil, and S. Ossokine, Phys. Rev. D **105**, 044035 (2022).
[19] A. Bonino, R. Gamba, P. Schmidt, A. Nagar, G. Pratten, M. Breschi, P. Rettegno, and S. Bernuzzi, Phys. Rev. D **107**, 064024 (2023).
[20] B. D. Lackey, M. Pürrer, A. Taracchini, and S. Marsat, Phys. Rev. D **100**, 024002 (2019).
[21] D. A. Godzieba, R. Gamba, D. Radice, and S. Bernuzzi, Phys. Rev. D **103**, 063036 (2021).
[22] M. Breschi, R. Gamba, S. Borhanian, G. Carullo, and S. Bernuzzi, arXiv:2205.09979.
[23] R. Gamba and S. Bernuzzi, Phys. Rev. D **107**, 044014 (2023).
[24] A. Matas *et al.*, Phys. Rev. D **102**, 043023 (2020).
[25] A. Gonzalez, R. Gamba, M. Breschi, F. Zappa, G. Carullo, S. Bernuzzi, and A. Nagar, Phys. Rev. D **107**, 084026 (2023).
[26] T. Damour and A. Nagar, Phys. Rev. D **77**, 024043 (2008).
[27] T. Damour, A. Nagar, E. N. Dorband, D. Pollney, and L. Rezzolla, Phys. Rev. D **77**, 084017 (2008).
[28] T. Damour, A. Nagar, M. Hannam, S. Husa, and B. Brügmann, Phys. Rev. D **78**, 044039 (2008).
[29] T. Damour and A. Nagar, Phys. Rev. D **79**, 081503 (2009).
[30] S. Hild, S. Chelkowski, and A. Freise, arXiv:0810.0604.
[31] S. Hild, S. Chelkowski, A. Freise, J. Franc, N. Morgado, R. Flaminio, and R. DeSalvo, Classical Quantum Gravity **27**, 015003 (2010).
[32] S. Hild *et al.*, Classical Quantum Gravity **28**, 094013 (2011).
[33] M. Evans *et al.*, arXiv:2109.09882.
[34] A. Nagar and P. Rettegno, Phys. Rev. D **104**, 104004 (2021).
[35] L. Pompili *et al.*, arXiv:2303.18039.
[36] A. Nagar, G. Riemenschneider, G. Pratten, P. Rettegno, and F. Messina, Phys. Rev. D **102**, 024077 (2020).
[37] A. Nagar, G. Pratten, G. Riemenschneider, and R. Gamba, Phys. Rev. D **101**, 024041 (2020).
[38] SXS Gravitational Waveform Database, https://data.black-holes.org/waveforms/index.html.
[39] L. T. Buchman, H. P. Pfeiffer, M. A. Scheel, and B. Szilagyi, Phys. Rev. D **86**, 084033 (2012).
[40] T. Chu, H. P. Pfeiffer, and M. A. Scheel, Phys. Rev. D **80**, 124051 (2009).
[41] D. A. Hemberger, G. Lovelace, T. J. Loredo, L. E. Kidder, M. A. Scheel, B. Szilágyi, N. W. Taylor, and S. A. Teukolsky, Phys. Rev. D **88**, 064014 (2013).
[42] M. A. Scheel, M. Giesler, D. A. Hemberger, G. Lovelace, K. Kuper, M. Boyle, B. Szilágyi, and L. E. Kidder, Classical Quantum Gravity **32**, 105009 (2015).
[43] J. Blackman, S. E. Field, C. R. Galley, B. Szilágyi, M. A. Scheel, M. Tiglio, and D. A. Hemberger, Phys. Rev. Lett. **115**, 121102 (2015).
[44] G. Lovelace, M. Boyle, M. A. Scheel, and B. Szilagyi, Classical Quantum Gravity **29**, 045003 (2012).
[45] G. Lovelace, M. Scheel, and B. Szilagyi, Phys. Rev. D **83**, 024010 (2011).
[46] A. H. Mroue, M. A. Scheel, B. Szilagyi, H. P. Pfeiffer, M. Boyle *et al.*, Phys. Rev. Lett. **111**, 241104 (2013).
[47] G. Lovelace *et al.*, Classical Quantum Gravity **32**, 065007 (2015).
[48] P. Kumar, K. Barkett, S. Bhagwat, N. Afshari, D. A. Brown, G. Lovelace, M. A. Scheel, and B. Szilágyi, Phys. Rev. D **92**, 102001 (2015).
[49] G. Lovelace *et al.*, Classical Quantum Gravity **33**, 244002 (2016).
[50] T. Chu, H. Fong, P. Kumar, H. P. Pfeiffer, M. Boyle, D. A. Hemberger, L. E. Kidder, M. A. Scheel, and B. Szilagyi, Classical Quantum Gravity **33**, 165001 (2016).
[51] V. Varma, S. E. Field, M. A. Scheel, J. Blackman, L. E. Kidder, and H. P. Pfeiffer, Phys. Rev. D **99**, 064045 (2019).
[52] A. Nagar, J. Healy, C. O. Lousto, S. Bernuzzi, and A. Albertini, Phys. Rev. D **105**, 124061 (2022).
[53] A. Nagar, T. Damour, C. Reisswig, and D. Pollney, Phys. Rev. D **93**, 044046 (2016).
[54] A. Nagar, G. Riemenschneider, and G. Pratten, Phys. Rev. D **96**, 084045 (2017).
[55] T. Damour, A. Nagar, and S. Bernuzzi, Phys. Rev. D **87**, 084035 (2013).
[56] Updated Advanced LIGO sensitivity design curve, https://dcc.ligo.org/LIGO-T1800044/public.
[57] A. Albertini, A. Nagar, P. Rettegno, S. Albanesi, and R. Gamba, Phys. Rev. D **105**, 084025 (2022).
[58] S. Albanesi, S. Bernuzzi, T. Damour, A. Nagar, and A. Placidi, arXiv:2305.19336.
[59] T. Damour, B. R. Iyer, and B. S. Sathyaprakash, Phys. Rev. D **57**, 885 (1998).
[60] P. Rettegno, F. Martinetti, A. Nagar, D. Bini, G. Riemenschneider, and T. Damour, Phys. Rev. D **101**, 104027 (2020).
[61] A. Nagar and A. Shah, Phys. Rev. D **94**, 104017 (2016).
[62] F. Messina, A. Maldarella, and A. Nagar, Phys. Rev. D **97**, 084016 (2018).
[63] A. Nagar, F. Messina, C. Kavanagh, G. Lukes-Gerakopoulos, N. Warburton, S. Bernuzzi, and E. Harms, Phys. Rev. D **100**, 104056 (2019).

[64] A. Albertini, A. Nagar, A. Pound, N. Warburton, B. Wardell, L. Durkan, and J. Miller, Phys. Rev. D **106**, 084061 (2022).
[65] A. Albertini, A. Nagar, A. Pound, N. Warburton, B. Wardell, L. Durkan, and J. Miller, Phys. Rev. D **106**, 084062 (2022).
[66] A. Bohé *et al.*, Phys. Rev. D **95**, 044028 (2017).
[67] R. Cotesta, A. Buonanno, A. Bohé, A. Taracchini, I. Hinder, and S. Ossokine, Phys. Rev. D **98**, 084028 (2018).
[68] T. Damour and A. Nagar, Phys. Rev. D **90**, 044018 (2014).
[69] E. Harms, S. Bernuzzi, A. Nagar, and A. Zenginoglu, Classical Quantum Gravity **31**, 245004 (2014).
[70] A. Nagar *et al.*, Phys. Rev. D **98**, 104052 (2018).
[71] S. Bernuzzi, A. Nagar, and A. Zenginoglu, Phys. Rev. D **83**, 064010 (2011).
[72] S. Bernuzzi, A. Nagar, and A. Zenginoglu, Phys. Rev. D **84**, 084026 (2011).
[73] T. Damour and A. Nagar, Phys. Rev. D **76**, 064028 (2007).
[74] J. Blümlein, A. Maier, P. Marquard, and G. Schäfer, Nucl. Phys. **B983**, 115900 (2022).
[75] A. Placidi, S. Albanesi, A. Nagar, M. Orselli, S. Bernuzzi, and G. Grignani, Phys. Rev. D **105**, 104030 (2022).
[76] S. Albanesi, A. Nagar, S. Bernuzzi, A. Placidi, and M. Orselli, Phys. Rev. D **105**, 104031 (2022).
[77] S. Albanesi, A. Placidi, A. Nagar, M. Orselli, and S. Bernuzzi, Phys. Rev. D **105**, L121503 (2022).
[78] A. M. Knee, I. M. Romero-Shaw, P. D. Lasky, J. McIver, and E. Thrane, Astrophys. J. **936**, 172 (2022).
[79] D. Bini and T. Damour, Phys. Rev. D **86**, 124012 (2012).
[80] A. Nagar, A. Bonino, and P. Rettegno, Phys. Rev. D **103**, 104021 (2021).
[81] T. Damour, F. Guercilena, I. Hinder, S. Hopper, A. Nagar, and L. Rezzolla, Phys. Rev. D **89**, 081503 (2014).
[82] S. Hopper, A. Nagar, and P. Rettegno, Phys. Rev. D **107**, 124034 (2023).
[83] R. Abbott *et al.* (LIGO Scientific, Virgo, and KAGRA Collaborations), arXiv:2111.03606 [Phys. Rev. X (to be published)].
[84] J. Yoo, V. Varma, M. Giesler, M. A. Scheel, C.-J. Haster, H. P. Pfeiffer, L. E. Kidder, and M. Boyle, Phys. Rev. D **106**, 044001 (2022).
[85] I. Harry, S. Privitera, A. Bohé, and A. Buonanno, Phys. Rev. D **94**, 024012 (2016).
[86] I. Harry, J. Calderón Bustillo, and A. Nitz, Phys. Rev. D **97**, 023004 (2018).
[87] C. García-Quirós, M. Colleoni, S. Husa, H. Estellés, G. Pratten, A. Ramos-Buades, M. Mateu-Lucena, and R. Jaume, Phys. Rev. D **102**, 064002 (2020).
[88] G. Pratten *et al.*, Phys. Rev. D **103**, 104056 (2021).
[89] T. Damour and A. Nagar, Phys. Rev. D **90**, 024054 (2014).
[90] S. Albanesi, A. Nagar, and S. Bernuzzi, Phys. Rev. D **104**, 024067 (2021).
[91] A. Nagar, T. Damour, and A. Tartaglia, Classical Quantum Gravity **24**, S109 (2007).
[92] S. Bernuzzi and A. Nagar, Phys. Rev. D **81**, 084056 (2010).
[93] B. J. Kelly and J. G. Baker, Phys. Rev. D **87**, 084004 (2013).
[94] A. Taracchini, A. Buonanno, G. Khanna, and S. A. Hughes, Phys. Rev. D **90**, 084025 (2014).
[95] M. Boyle *et al.*, Classical Quantum Gravity **36**, 195006 (2019).
[96] M. Khalil, A. Buonanno, J. Steinhoff, and J. Vines, Phys. Rev. D **106**, 024042 (2022).
[97] D. Chiaramello and A. Nagar, Phys. Rev. D **101**, 101501 (2020).
[98] S. Bernuzzi, A. Nagar, T. Dietrich, and T. Damour, Phys. Rev. Lett. **114**, 161103 (2015).
[99] S. Akcay, S. Bernuzzi, F. Messina, A. Nagar, N. Ortiz, and P. Rettegno, Phys. Rev. D **99**, 044051 (2019).
[100] https://bitbucket.org/eob_ihes/teobresums/src/master/.
[101] M. Breschi, R. Gamba, and S. Bernuzzi, Phys. Rev. D **104**, 042001 (2021).
[102] G. Ashton *et al.*, Astrophys. J. Suppl. Ser. **241**, 27 (2019).
[103] C. Biwer, C. D. Capano, S. De, M. Cabero, D. A. Brown, A. H. Nitz, and V. Raymond, Publ. Astron. Soc. Pac. **131**, 024503 (2019).